

**UCLA**

**UCLA Electronic Theses and Dissertations**

**Title**

SnO<sub>2</sub>/Graphene Nanocomposites as High-Capacity Anode Materials for Lithium-Ion Batteries: Synthesis and Electrochemical Performance

**Permalink**

<https://escholarship.org/uc/item/41g3q26f>

**Author**

Zhu, Xiuming

**Publication Date**

2018

Peer reviewed|Thesis/dissertation

UNIVERSITY OF CALIFORNIA

Los Angeles

SnO<sub>2</sub>/Graphene Nanocomposites as High-Capacity Anode Materials for Lithium-Ion  
Batteries: Synthesis and Electrochemical Performance

A thesis submitted in partial satisfaction  
of the requirements for the degree Master of Science  
in Materials Science and Engineering

by

Xiuming Zhu

2018

© Copyright by

Xiuming Zhu

2018

## ABSTRACT OF THE DISSERTATION

SnO<sub>2</sub>/Graphene Nanocomposites as High-Capacity Anode Materials for Lithium-Ion  
Batteries: Synthesis and Electrochemical Performance

by

Xiuming Zhu

Master of Science in Materials Science and Engineering

University of California, Los Angeles, 2018

Professor Bruce S. Dunn, Chair

Lithium ion batteries as a power source are the most commonly used in the electronic devices and electric vehicles (EV) for grid-energy storage. Anode materials with high specific capacity for lithium ion batteries have been developed in recent years. SnO<sub>2</sub> has also been considered as a promising candidate to serve as the anode material for lithium ion batteries due to its high theoretical capacity. But the volume expansion effect results in the degradation of active material and limits the complete realization of theoretical capacity. Graphene has recently become one of the most promising matrices for high-capacity anode materials, due to good electrical conductivity, outstanding mechanical flexibility and high theoretical capacity. In this paper, the nanocomposites of SnO<sub>2</sub> and graphene as anode materials for lithium ion batteries were facilely synthesized through hydrothermal method. The design of SnO<sub>2</sub>/graphene nanocomposites could significantly improve the electrochemical performance by



increasing electrical conductivity and buffering volume expansion. It is noteworthy that the quality and structural design of graphene is very important to improve the electrochemical performance for SnO<sub>2</sub>-based materials. Therefore, on the one hand, a new method to prepare highly dispersible edge-selectively oxidized graphene was reported in this paper. On the other hand, we designed a novel three-dimensional graphene named flower-like graphene tube. Furthermore, characterization and electrochemical performance of these materials were also studied by various technologies.

The thesis of Xiuming Zhu is approved.

Yunfeng Lu

Sarah H. Tolbert

Bruce S. Dunn, Committee Chair

University of California, Los Angeles

2018

# Table of Contents

<b>1</b>	<b>Introduction</b> .....	<b>vii</b>
<b>1.1</b>	<b>Introduction of Lithium-ion batteries</b> .....	<b>1</b>
1.1.1	Development history .....	1
1.1.2	Structure and working principle .....	2
1.1.3	Pros and cons of lithium ion battery.....	3
1.1.4	Application of lithium ion battery .....	4
<b>1.2</b>	<b>Introduction of anode materials</b> .....	<b>6</b>
<b>1.3</b>	<b>Introduction of Sn anode materials</b> .....	<b>10</b>
1.3.1	Properties of Sn anode materials .....	10
1.3.2	Regular improvement solutions .....	12
<b>1.4</b>	<b>Introduction of SnO<sub>2</sub> anode materials</b> .....	<b>15</b>
1.4.1	Properties of SnO <sub>2</sub> anode materials .....	15
1.4.2	Regular improvement solution .....	15
<b>1.5</b>	<b>Introduction of Graphene</b> .....	<b>17</b>
<b>1.6</b>	<b>Ideas in this thesis</b> .....	<b>20</b>
<b>2</b>	<b>Experiment</b> .....	<b>22</b>
<b>2.1</b>	<b>Chemicals</b> .....	<b>22</b>
<b>2.2</b>	<b>Instrument</b> .....	<b>23</b>
<b>2.3</b>	<b>Experiments</b> .....	<b>24</b>
2.3.1	EOG-based SnO <sub>2</sub> materials.....	24
2.3.2	FGT-based SnO <sub>2</sub> materials.....	25
<b>2.4</b>	<b>Materials characterization and electrochemical performance tests</b> .....	<b>27</b>
2.4.1	Materials characterization.....	27
2.4.2	Electrochemical performance tests.....	28

<b>3</b>	<b>Results and Discussion</b> .....	<b>30</b>
<b>3.1</b>	<b>3.1 EOG-based SnO<sub>2</sub> materials</b> .....	<b>30</b>
3.1.1	Characterization and electrochemical tests of EOG .....	30
3.1.2	Characterization and electrochemical test results of SnO <sub>2</sub> nanoparticles and SnO <sub>2</sub> /EOG nanocomposites .....	37
<b>3.2</b>	<b>FGT-based SnO<sub>2</sub> nanomaterials</b> .....	<b>45</b>
3.2.1	Characterization results of FGT .....	45
3.2.2	Characterization and electrochemical test results of SnO <sub>2</sub> -FGT nanocomposites ..	50
<b>4</b>	<b>Conclusion</b> .....	<b>57</b>

## List of Figures

Figure 1.1 Schematic for working principle in lithium ion battery. ....	2
Figure 1.2 (a) Characterization of the main three kinds of EVs: light EV, PHEV and full EV, in terms of performance and battery properties. (b) Ragone plot.....	6
Figure 1.3 The compositional dependence of the densities of Li-Sn alloys as computed from crystallographic data. ....	11
Figure 1.4 Characteristic charge curve of electroplated Sn in 1 M LiClO <sub>4</sub> /PC, $i = 0.025$ mA/cm <sup>-2</sup> . [60] .....	12
Figure 1.5 TEM images for tin-carbon composites with different structures. ....	14
Figure 1.6 The TEM image of (a) SnO <sub>2</sub> nanoparticles, (b) SnO <sub>2</sub> nanorods, (c) hollow SnO <sub>2</sub> with size of 100 nm, (d) carbon-coated SnO <sub>2</sub> nanocolloids. ....	17
Figure 1.7 Schematic diagram of graphene. ....	18
Figure 3.1 Schematic for synthesis process of EOG.....	31
Figure 3.2 (a) XRD pattern of graphite, edge oxidized graphite and FeCl <sub>3</sub> intercalated edge oxidized graphite. SEM images of (b) graphite, (c) edge oxidized graphite, (d) FeCl <sub>3</sub> intercalated edge oxidized graphite, (e) FeCl <sub>3</sub> intercalated edge oxidized graphite exfoliated by H <sub>2</sub> O <sub>2</sub> for the first time and (f) single edge oxidized graphene (EOG) sheet. ....	32
Figure 3.3 XRD patterns of graphite, edge oxidized graphite and edge oxidized exfoliated graphene.....	33
Figure 3.4 Raman spectra of graphite, edge part of exfoliated graphene and central part of exfoliated graphene.....	35

Figure 3.5 (a) (b) SEM images of EOG with different scalar of 1 $\mu\text{m}$ and 500 nm respectively. (c) TEM image of EOG. (d) HRTEM image of EOG.....	36
Figure 3.6 Cycle performance of EOG at different current densities from 0.1 A $\text{g}^{-1}$ to 1 A $\text{g}^{-1}$ .....	37
Figure 3.7 Schematic for synthesis process of bare $\text{SnO}_2$ nanoparticles and $\text{SnO}_2/\text{EOG}$ nanocomposites. ....	38
Figure 3.8 XRD patterns of bare $\text{SnO}_2$ nanoparticles and $\text{SnO}_2/\text{EOG}$ nanocomposites. ....	39
Figure 3.9 (a) TEM image and (b) HRTEM image for $\text{SnO}_2$ nanoparticles. (c) TEM image and (d) HRTEM image for $\text{SnO}_2/\text{EOG}$ nanocomposites.....	40
Figure 3.10 Discharge/charge profile of 1 <sup>st</sup> , 2 <sup>nd</sup> and 50 <sup>th</sup> cycle for (a) bare $\text{SnO}_2$ nanoparticles and (b) $\text{SnO}_2/\text{EOG}$ nanocomposites.....	41
Figure 3.11 Cycle performance of bare $\text{SnO}_2$ nanoparticles and $\text{SnO}_2/\text{EOG}$ nanocomposites at constant current density of 0.1 A $\text{g}^{-1}$ . ....	42
Figure 3.12 Cycle performance of bare $\text{SnO}_2$ nanoparticles and $\text{SnO}_2/\text{EOG}$ nanocomposites at different current densities from 0.1 A $\text{g}^{-1}$ to 1 A $\text{g}^{-1}$ . ....	43
Figure 3.13 Electrochemical impedance spectra of bare $\text{SnO}_2$ nanoparticles and $\text{SnO}_2/\text{EOG}$ nanocomposites. The inset part is magnification of the original spectra. ....	44
Figure 3.14 Schematic for synthesis process of flower-like graphene tube (FGT) from flower-like MgO tube template. ....	46
Figure 3.15 XRD pattern for flower-like MgO tube, flower-like MgO@graphene and flower-like graphene tube (FGT). ....	47

Figure 3.16 (a) SEM image for flower-like MgO hierarchical tube. (b-d) SEM mapping for flower-like MgO hierarchical tube, (c) and (d) respectively refer to the element distribution of magnesium (Mg) and oxygen (O) among the selected sample in (b). .....	48
Figure 3.17 (a) SEM image for MgO@graphene intermediate. (b-f) SEM mapping for MgO@graphene intermediate, (c), (d), (e) and (f) respectively refer to the element distribution of magnesium (Mg), oxygen (O), carbon (C) and nitrogen (N) among the selected sample in (b). .....	49
Figure 3.18 SEM images for flower-like graphene tube (FGT) in different magnifications. .....	50
Figure 3.19 Schematic for synthesis process of SnO <sub>2</sub> -FGT nanocomposites.....	51
Figure 3.20 XRD pattern for SnO <sub>2</sub> -FGT nanocomposites. ....	52
Figure 3.21 SEM images for SnO <sub>2</sub> -FGT nanocomposites in different magnifications....	53
Figure 3.22 Discharge/charge profile of 1 <sup>st</sup> , 2 <sup>nd</sup> and 50 <sup>th</sup> cycle for SnO <sub>2</sub> -FGT nanocomposites. ....	54
Figure 3.23 Cycle performance of SnO <sub>2</sub> -FGT nanocomposites at different current densities of 0.1 A g <sup>-1</sup> and 1.0 A g <sup>-1</sup> . ....	55
Figure 3.24 Cycle performance SnO <sub>2</sub> -FGT nanocomposites at different current densities from 0.1 A g <sup>-1</sup> to 1 A g <sup>-1</sup> . ....	56

## List of Tables

Table 2-1 Table of chemicals. ....	22
Table 2-2 Table of instruments.....	23



# 1 Introduction

Today with fast economic development, the world faces intense energy challenge since traditional energy sources like petrol and coal are decreasing and environmental pollution becomes increasingly severe. To solve this problem, scientists are exploring new types of clean energy such as solar and wind energy. However, due to their discontinuity and dispersal, it is necessary to improve the technology for energy transformation and storage. Among variable methods of chemical energy storage in our society, lithium ion battery (LIB) is most popular and efficient with benefits of high capacity, small volume, long lifetime and high security. <sup>[1-3]</sup>

## 1.1 Introduction of Lithium-ion batteries

### 1.1.1 Development history

LIBs are based on lithium metal electrode batteries, which use lithium or lithium alloys as anode materials. But the disadvantages of lithium batteries are quite obvious. On one hand, during discharge process, lithium will sediment on anode producing dendritic lithium, which can penetrate battery separator and cause short circuit. On the other hand, lithium is so active that it can react with any organic and inorganic chemicals, like electrolyte, resulting in low charge and discharge efficiency.

In 1977, Samar Basu from University of Pennsylvania found the property of electrochemical intercalation of lithium in graphite. <sup>[4-5]</sup> This led to the invention of a workable lithium intercalated graphite electrode at Bell labs ( $\text{LiC}_6$ ) to provide an alternative to the lithium metal electrode battery. <sup>[6]</sup> In 1980, John Goodenough

demonstrated lithium cobalt oxide ( $\text{LiCoO}_2$ ) as cathode material. [7] And in the same year, Rachid Yazami also confirmed the reversible electrochemical intercalation of lithium in graphite and firstly used solid electrolyte to reduce the reaction between electrode and liquid electrolyte. [8]  $\text{LiCoO}_2$  and graphite are the most commonly-used electrode materials in today's commercial LIB. Sony and Asahi Kasei released the first commercial lithium ion battery in 1991.

### 1.1.2 Structure and working principle

As shown in Figure 1.1, LIB usually consists of anode, cathode, separator, electrolyte and outer-shell. The main LIB full cell reactions are reversible Lithium ion de-intercalation/intercalation process between cathode and anode material.

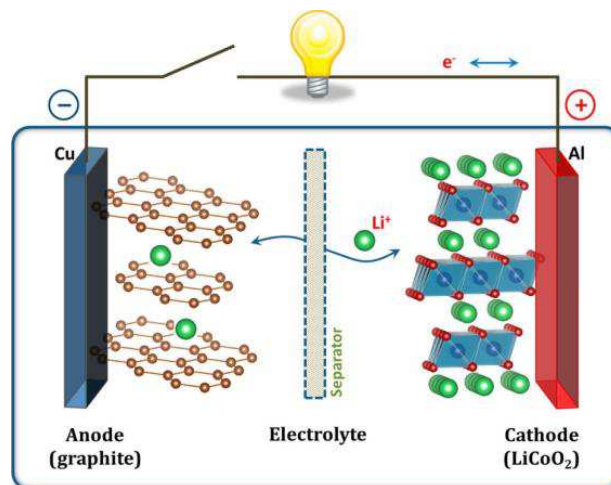


Figure 1.1 Schematic for working principle in lithium ion battery.

The anode and cathode are made of materials that can be reversibly intercalated and deintercalated. For commercial use, we choose lithium metal oxide ( $\text{LiMO}_2$ ), including  $\text{LiCoO}_2$  and  $\text{LiFePO}_4$ , as cathode material. Based on the property that  $\text{LiCoO}_2$  has high energy density but also presents safety problem when damaged,  $\text{LiCoO}_2$  is commonly

used in handheld electronics like cell phone and laptop. While  $\text{LiFePO}_4$  shows lower energy capacity but longer life time and better safety performance, so  $\text{LiFePO}_4$  is applied on electric tools, medical equipment and other roles. For anode materials, graphite is the most popular materials due to its low cost. Also in order to improve the electrochemical performance of LIB, scientists have done some modification of graphite. For example, carbon nanotubes, as an allotrope of graphite, have already shown competitive performance as lithium storage material. Especially when combined with other improved high-capacity anode materials, carbon nanotubes can serve as backbone and effective buffering component to decrease the degradation effect resulting from impressive volume change during discharging and charging process. <sup>[9]</sup>

Other than cathode and anode, electrolyte also plays an important role in transporting lithium ions between cathode and anode. High purity electrolyte comprised of lithium salt, including  $\text{LiPF}_6$ ,  $\text{LiClO}_4$  and  $\text{LiAsF}_6$ , solved in organic solution like EC (Ethylene carbonate), DEC (Diethyl Carbonate), DMC (Dimethyl Carbonate) and PC (Propylene carbonate) is a key component of LIB.

### 1.1.3 Pros and cons of lithium ion battery

Compared with other rechargeable batteries, such as lead-acid cell, nickel-cadmium cell and nickel-metal hydride battery, LIB owns very impressive advantages: <sup>[10]</sup>

1. High working voltage and energy capacity. Working voltage of LIB is around 3.6 V, while nickel-cadmium cell and nickel-metal hydride battery are about 1.2 V. High working voltage can give benefit to combined batteries to obtain higher voltage with fewer batteries.

2. Small volume, low weight, but high energy density. Usually energy density of LIB can be 2 times of nickel-cadmium cell. When compared with nickel-metal hydride battery with same energy density, LIB is 30% smaller and 50% lighter. Hence, LIB is more convenient when used in carry-on electronics.

3. Long cycle life. Statistically, LIB with  $\text{LiCoO}_2$  as cathode and graphite as anode can complete at least 500 charge-discharge cycles.

4. Wide working temperature. LIB can work properly during  $-20^\circ\text{C}$  and  $60^\circ\text{C}$ , especially when the temperature is as low as  $-20^\circ\text{C}$ , LIB still can release 90% of its capacity.

5. Less pollution. LIB contains less of toxic metals, such as lead and cadmium. The elements in LIB include nickel, cobalt, iron and copper, which are considered safe. Therefore, LIB will not pollute the earth or water even buried with normal trash.

Although LIB has many advantages as stated above, disadvantages or risks should not be neglected. The most severe problem is risk of overcharge and discharge, which may result in leakage, fire or explosion. The reason for this is that during use, anode produces heat and cathode may produce oxygen. The additional oxygen, which should not occur in battery, may cause damage to the whole cell and even short circuit. Short circuit of a battery is the most common way to cause the battery to overheat and possibly to catch a fire. Then adjacent battery can also overheat and fail.




#### 1.1.4 Application of lithium ion battery

The techniques of LIB used in portable electronics like cell phone, pad and laptop have become more and more mature. But new requests are being pushed forward with the

development of electric vehicles (EVs), which represents the energy challenge the world is facing. There is general agreement among people that we need to shift ground transportation from using internal combustion engines (ICEs) to sustainable energy sources. [11] Although fuel cells (FCs) can provide the highest energy density, due to its operation problems related to electro-catalysis, LIB is the only choice for EV application.

Figure 1.2 (a) demonstrates three kinds of commercial EVs divided by the depth of pure electrical propulsion. According to their separate battery data, we can find that the more our EV depends on electrical propulsion, the more energy density and power density we need. Figure 1.2 (b) shows Ragone plots (power density vs. energy density) for three mainly used rechargeable batteries in EV: lead-acid battery, Ni-MH battery and LIB.

Figure 2b confirms that today only LIB is suitable for the development of EV.

a						
Modes of operation		battery capacity needed, kWh	Energy density, Wh/kg	Weight of battery, Kg	Speed, kilometres per hour	Distance on one charge, kilometres
	Hybrid	<3	40-50 (Ni-MH)	60 (Ni-MH)	100+	15
	Plug in Hybrid	5.6-18	90-100 (Li-ion)	60-200 (Li-ion)	100+	10-60
	Full EV	35-54	90-100 (Li-ion)	450 (Li-ion)	>100	150-200

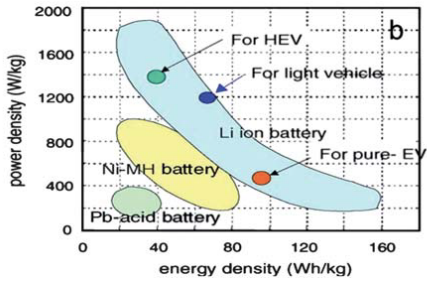


Figure 1.2 (a) Characterization of the main three kinds of EVs: light EV, PHEV and full EV, in terms of performance and battery properties. (b) Ragone plot.

## 1.2 Introduction of anode materials

Great effort has been spent on developing high quality anode materials. Ideal anode materials are expected to have following properties:

1. The oxidation-reduction potential of anode when intercalated by lithium ions should be as low as possible. This can lead to high output potential.
2. The intercalation and de-intercalation process should be reversible and make impact on main structure of anode material as little as possible. This can ensure good cycle performance.
3. In order to obtain higher capacity, there should be more lithium ions able to intercalate into anode material.
4. The intercalated material should have high electronic conductivity and ionic conductivity to reduce electrode polarization so that the material can charge and discharge under high current.
5. The material should have good facial structure leading to producing high-quality solid-electrolyte interface (SEI).
6. The intercalated material should maintain chemical stability during the full working potential range, which means the material should not react with electrolyte after formation of SEI.

7. From the aspect of commercial use, the main material should have low price to decrease production cost and not make pollution to environment.

Until now, scientists are still exploring variety of anode materials to find suitable replacement of graphite which conquers most of LIB market but gets restriction of its relatively low theoretical capacity. For simplification, we divide common anode materials into three main group: <sup>[12]</sup>

#### 1. Insertion/de-insertion materials

Insertion/de-insertion materials are those materials charged and discharged only by absorbing lithium ions in lattice matrix instead of reaction or performing alloys. Usually these materials undergo less volume expansion than other kinds of materials.

##### a. Carbon-based materials

Carbon-based materials were the first kind of material applied in lithium ion batteries. <sup>[13-18]</sup> Carbon-based materials can be divided into soft carbon (ordered carbon), hard carbon (disordered carbon) and nanostructured carbon, based on the arrangement of single graphene sheets. <sup>[19]</sup> Graphene will be introduced in the following part. Soft carbon, also known as graphitizable carbon, where crystallites are stacked almost in the same direction, is quite popular in commercial battery. However, the use of soft carbon is limited to low power required devices due to its low reversible capacity (350-370 mAh g<sup>-1</sup>). According to Dahn et al. <sup>[20]</sup>, hard carbon is believed to have higher capacity than graphite because hard carbon contains a large fraction of graphene sheet, whose capacity can be obtained up to 740 mAh g<sup>-1</sup> when lithium ions are absorbed on both sides of graphene sheets. In addition, in the hard carbon with small crystallite size,

lithium ions are not only inserted between graphitic layers, but also absorbed at the edge of the graphitic layer and the surface of the crystallite. <sup>[21]</sup> Among nanostructured carbon, carbon nanotubes (CNTs), composed of cylindric single or multiple rolled graphene sheets, are proposed to be alternative of graphite because there are more sites in CNTs for intercalation of lithium ions, including inter-shell, inter-tube and inner core.

Carbon-based materials are recognized as suitable anode materials due to their considerable features, especially stability in thermal, chemical and electrochemical environment. Based on this property, carbon is usually used as coating material on active anode materials because the lithium salt  $\text{LiPF}_6$  in electrolyte can react with electrode resulting in the formation of a thick layer, known as Solid Electrolyte Interface (SEI). The formation of SEI will cause degradation of both active materials in electrode and electrolyte. Therefore, the use of carbon coating can prevent the formation of SEI and surface oxidation.

#### b. Titanium based oxides

Titanium based oxides have attracted scientists because of their low cost, low toxicity and low volume expansion (2-3%) during charge and discharge. Moreover, titanium based oxides have good rate performance and cycle life. <sup>[22]</sup> The drawback of this kind of materials limiting their commercial usage is their relatively low theoretical capacity (in the range of 170-330 mAh  $\text{g}^{-1}$ ) and low electronic conductivity. To mitigate this problem, scientists choose to combine them with carbon based materials, such as CNT and graphene, or metal oxides with higher capacity. <sup>[23-26]</sup>

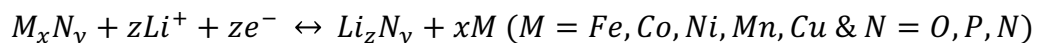


## 2. Alloy/de-alloy materials

Fast-developing electrical devices today requires LIB with higher capacity and energy density. Anode materials that can satisfy these requirements are silicon (Si), germanium (Ge), tin (Sn) and tin oxides, which can react with lithium under alloy/de-alloy mechanism. Si has the highest gravimetric capacity ( $4200 \text{ mAh g}^{-1}$ ,  $\text{Li}_{22}\text{Si}_5$ ) and volumetric capacity ( $9786 \text{ mAh cm}^{-3}$ ) among anode materials. <sup>[27]</sup> Also, Si is the second abundant element in earth so that Si is environmentally friendly. However, the large volume modification ( $\sim 400\%$ ) and formation of Si compound in SEI prevent Si from commercial application. <sup>[28-31]</sup> Ge is also a widely studied material, with capacity up to  $1623 \text{ mAh g}^{-1}$ . <sup>[32]</sup> Ge has more advantages than Si, such as higher intrinsic electrical conductivity ( $10^4$  times higher than Si) and faster lithium diffusion (400 times faster than Si at room temperature). <sup>[33-36]</sup> The disadvantage of Ge is the same as discussed in Si. The promising improvement methods include minimizing the particle size to nanoscale and combining active material with inactive matrix materials. The details of Sn and  $\text{SnO}_2$  anode materials will be discussed in the following introduction of Sn anode materials.

## 3. Conversion materials

Conversion materials refer to transition metal compounds, including oxides, phosphides and nitrides. When applied in LIBs as anode materials, conversion materials undergo oxidation/reduction reaction and composition/decomposition of lithium compounds during charging/discharging process. The reaction can be simplified as the following equation:



Although these materials, such as iron oxide <sup>[37-42]</sup> and cobalt oxide <sup>[43-48]</sup>, own higher theoretical capacity (500-1000 mAh g<sup>-1</sup>) than graphite, they also suffer from poor cycling performance due to low electrical conductivity and lithium diffusion, high volume change and iron aggregation. Many researchers are working on modification of particle size, morphology and porosity to enhance their lithium diffusion speed. <sup>[49]</sup> Also in order to improve their electrical conductivity, most scientists choose to coat the materials with carbon or synthesis carbon-based compounds. <sup>[50]</sup>

## 1.3 Introduction of Sn anode materials

### 1.3.1 Properties of Sn anode materials

According to our deviation above, tin belongs to alloy/de-alloy anode materials and has been studied for many years. <sup>[51-56]</sup> When tin is during charge and discharge, it will form intermetallics with lithium ions. Figure 1.3 shows some common Li-Sn intermetallics of different compositions, including Li<sub>22</sub>Sn<sub>5</sub>, Li<sub>7</sub>Sn<sub>2</sub>, Li<sub>13</sub>Sn<sub>5</sub>, Li<sub>5</sub>Sn<sub>2</sub>, Li<sub>7</sub>Sn<sub>3</sub>, LiSn and Li<sub>2</sub>Sn<sub>5</sub>. <sup>[57]</sup> The capacity of Sn anode materials depends on how much lithium ions can form intermetallis with them, which is the composition of Li-Sn intermetallics. The higher the ratio of Li to Sn, the higher the capacity. Therefore, the highest theoretical capacity of Sn anode materials is about 994 mAh/g based on Li<sub>22</sub>Sn<sub>5</sub>, which is almost 3 times of theoretical capacity of graphite. <sup>[58]</sup>

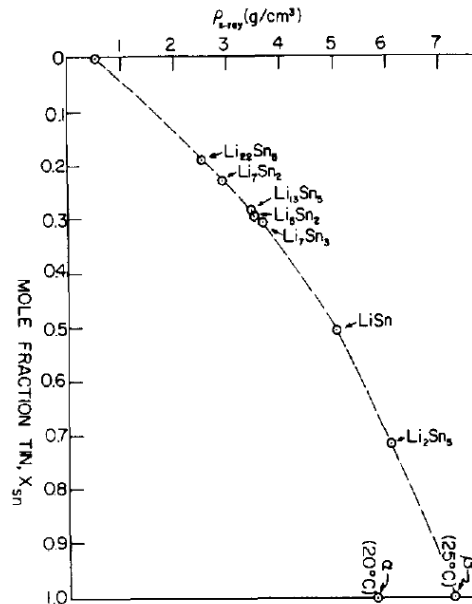


Figure 1.3 The compositional dependence of the densities of Li-Sn alloys as computed from crystallographic data.

Also from Figure 1.3 where the density of  $\text{Li}_{22}\text{Sn}_5$  is only 30% of Sn, the density of intermetallics changes excessively with composition. This is due to the fact that lithium owns the smallest density of  $0.534 \text{ g/cm}^3$  among all kinds of condensed elements, while tin has density of  $7.365 \text{ g/cm}^3$ . The extremely large density change between tin and intermetallics leads to impressive volume change when tin is under lithiation. The lithium-rich intermetallics are brittle and can be easily pulverized due to great mechanical stress and strain driven by the large volume change. This could result in insufficient cycling performance because of the loss of electronic connection between particles and between particles and current collector, and finally anode degradation or even fail. <sup>[59]</sup> Hence, we are trapped in a dilemma, where higher capacity requires more lithium intercalation while more lithium intercalation causes more excessive volume

change. This problem has been proposed by scientist for several decades but still the main challenge for commercialization of tin anode materials.

### 1.3.2 Regular improvement solutions

In early years, in order to achieve the balance between ideal capacity and reduce volume change, scientists usually dealt with this by controlling working voltage or particle size.

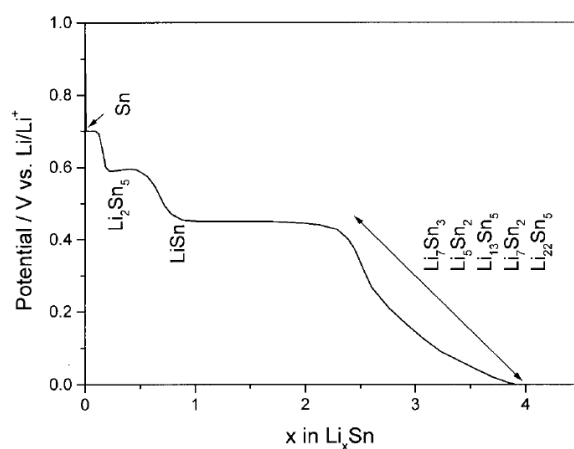


Figure 1.4 Characteristic charge curve of electroplated Sn in 1 M LiClO<sub>4</sub>/PC,  $i = 0.025 \text{ mA/cm}^2$ .

[60]

As shown in Figure 1.4, the potential of Li-Sn intermetallics vs Li/Li<sup>+</sup> decreases when the lithium content increases. Therefore, the method of controlling working voltage is to close the potential window when cycling to form intermetallic with lower lithium content.

It has been confirmed that reducing the particle size of active materials to the nanometer range (<100nm) can significantly improve their cycling performance, which can be attributed to the ability of nanosized particles to accommodate large stress and strain. [61-62] According to Hall-Petch relation, the increase in yield stress is inversely

proportional to the square root of the grain size. The plastic deformation of metal and alloy is usually controlled by the motion of dislocation. Also it is believed that grain boundaries can hinder dislocation activity so that small grain size makes plastic deformation more difficult. Therefore, nanosized particles are able to sustain great stress and strain caused by volume change.<sup>[63]</sup> Moreover, high density of grain boundaries in nanosized particles can provide more sites for lithium intercalation, reducing total volume expansion.<sup>[64]</sup> However, the problems of nanosized particles are also unavoidable. Large surface area of nanosized particles leads to more reactions between active anode material and electrolyte to form SEI, which may result in self-discharge and poor cycling life.

To overcome the disadvantage brought with nanosized particle and also improve the mechanical property to buffer the volume change, scientists choose to introduce a second phase to active materials. The second phase served as matrix phase hosting active materials should ensure the electric and ionic conductivity of the whole anode.<sup>[65]</sup> Carbon-based materials have been demonstrated experimentally to be able to improve the cycling performance of nanosized. In fact, many metals can react with carbon to form carbides, but tin has no solubility or reaction with carbon, which makes it possible to design multiple different structures of carbon-tin composites.<sup>[59]</sup> The mechanism of buffering volume change is suggested that the carbon coating exerts a compressive stress on the active particle with opposite direction of the force produced by volume expansion during lithiation.<sup>[66]</sup> In addition, the improved cycling performance can be attributed to the improved electric and ionic conductivity. Moreover, the carbon coating

can suppress the formation of SEI, reducing the reaction between active materials and electrolyte.

Scientists have been working with carbon-tin composites with different structures for many years. For example, Figure 1.5 (a) shows amorphous carbon-coated tin with first charge and discharge capacities of 789 mAh/g and 681 mAh/g respectively. <sup>[67]</sup> The calculated ratio of irreversible capacity was 14%, while that of Sn particles only was calculated to be 7% from the discharge and charge capacities of 631 mAh/g and 587 mAh/g. Moreover, after 50 cycles, the capacity was kept at 664 mAh g<sup>-1</sup> at 0.5 C. Another commonly studied structure, tin-nanoparticles encapsulated in elastic hollow carbon spheres, is shown in Figure 1.5 (b). <sup>[68]</sup> The electrochemical performance of this material suggests that even after 100 cycles, the specific capacity is remained higher than 550 mAh g<sup>-1</sup>. Although the carbon shell of this structure is thick and the content of Sn is only 24%, the specific capacity is about 400 mAh g<sup>-1</sup>. The novel structure of tin-filled carbon nanotubes is presented in Figure 1.5 (c). <sup>[69]</sup> The cycling result shows that the 40th-cycle capacity at 0.1 C is 844 mAh g<sup>-1</sup> at 0.1C, which exceeds many other Sn-based materials.

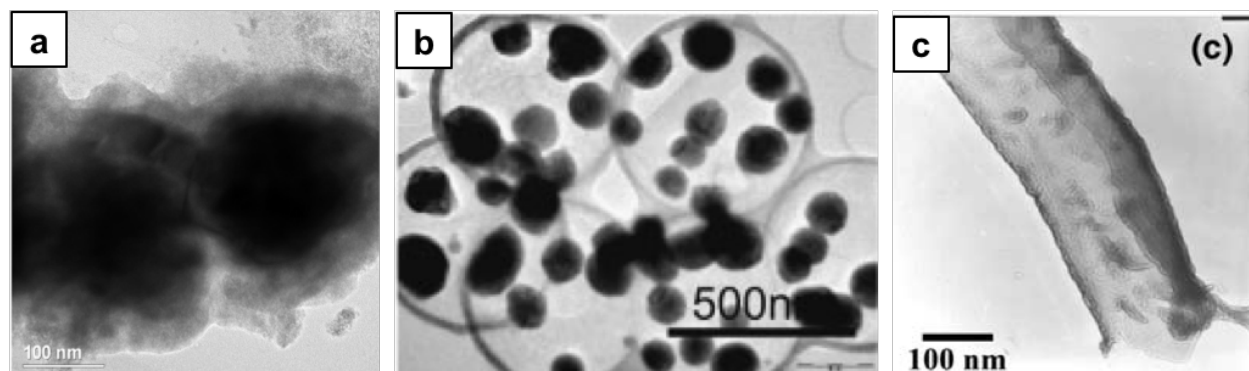
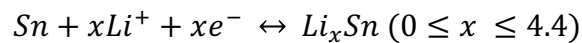
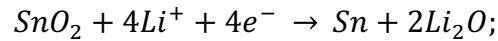


Figure 1.5 TEM images for tin-carbon composites with different structures.

## 1.4 Introduction of SnO<sub>2</sub> anode materials

### 1.4.1 Properties of SnO<sub>2</sub> anode materials

SnO<sub>2</sub> is belong to alloy/de-alloy anode materials. When SnO<sub>2</sub> is used in LIB, the electrochemical mechanism includes irreversible and reversible steps: <sup>[70]</sup>



The overall corresponding theoretical capacity can reach up to 1491 mAh g<sup>-1</sup>, but when it reaches to the second cycle, the capacity is reduced to 783 mAh g<sup>-1</sup> because of the first irreversible reaction where SnO<sub>2</sub> is reduced to Sn. <sup>[71]</sup> So 783 mAh g<sup>-1</sup> is widely considered as the actual theoretical capacity, which is still twice the capacity of graphite.

Widespread use of SnO<sub>2</sub> is hampered by two major problems: large initial irreversible capacity loss and poor cycling performance. The large irreversible capacity loss after the first cycle is the result of the first reduction reaction, while the poor cycling performance is attributed to the large volume change during lithium ion insertion and extraction. When SnO<sub>2</sub> is reduced to Sn after the first cycle, the charge and discharge process is similar to that of Sn anode materials as discussed in the former part, where the large density difference between Sn and Li leads to the impressive volume expansion, ultimately resulting in their disintegration or pulverization.

### 1.4.2 Regular improvement solution

According to Sn anode materials, downsizing the particles to nanoscale can improve the cycling performance. In this regard, Zheng et al. studied SnO<sub>2</sub> nanoparticles (~20nm)

and SnO<sub>2</sub> nanorods (diameter 500nm, length 2-3 μm) as anode materials for LIB. Figure 1.6 (a) and (b) are TEM images of SnO<sub>2</sub> nanoparticles and nanorods respectively. <sup>[72]</sup>

The cyclic results show that in the initial four cycles, nanoparticles electrode presents specific capacities more than 1000 mAh g<sup>-1</sup>, while the capacities of SnO<sub>2</sub> nanorods are about 700 mAh g<sup>-1</sup>. The large difference between their initial performance is due to their various difficulties for lithium intercalation and deintercalation. During the following ten cycles, the capacities of SnO<sub>2</sub> nanoparticles reduce faster than that of SnO<sub>2</sub> nanorods also because the hardness of lithium transportation in SnO<sub>2</sub> nanorods attenuates the degradation of the active materials.

It has also been confirmed that modification of morphology, such as porous nanostructures and hollow structure, can balance the volume change during charging and discharging. Hollow structure is one of the most promising ways to overcome the pulverization of SnO<sub>2</sub> materials. It is believed that hollow sphere is stronger than the solid sphere with same weight. <sup>[73]</sup> Kim et al. used sacrificed template method to synthesize hollow SnO<sub>2</sub> with diameter range from 25 nm to 100 nm. <sup>[74]</sup> The TEM image of hollow SnO<sub>2</sub> with size of 100 nm is shown in Figure 1.6 (c). The electrochemical cycling results demonstrate that hollow SnO<sub>2</sub> with smallest size remains the highest capacity about 750 mAh g<sup>-1</sup> after 50 cycles approaching its theoretical capacity.

Considering the importance of carbon based materials in LIB, researchers proceed further development of combining them with SnO<sub>2</sub> active materials, such as carbon-coated SnO<sub>2</sub>, SnO<sub>2</sub>/CNT and SnO<sub>2</sub>/graphene. The existence of carbon in the complex can not only increase the electrical conductivity but also buffer the volume change. Lou et al. reported a simple hydrothermal method using glucose as carbon resource to



synthesize monodisperse carbon-coated SnO<sub>2</sub> nanocolloids as shown in Figure 1.6 (d).<sup>[75]</sup> The thickness of the carbon shell can be controlled by monitor the glucose concentration. They found that the complex material can keep the capacity of 440 mAh g<sup>-1</sup> after more than 100 cycles.

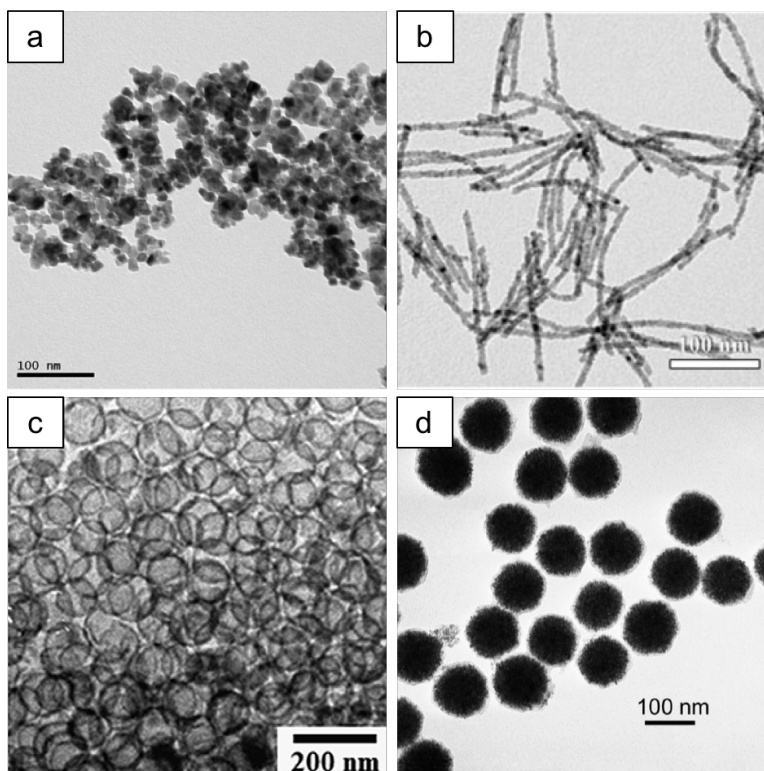


Figure 1.6 The TEM image of (a) SnO<sub>2</sub> nanoparticles, (b) SnO<sub>2</sub> nanorods, (c) hollow SnO<sub>2</sub> with size of 100 nm, (d) carbon-coated SnO<sub>2</sub> nanocolloids.

## 1.5 Introduction of Graphene

Graphene is a single layer carbon arranged in hexagonal lattice, which is a honeycomb like structure as shown in Figure 1.7. Graphene was firstly obtained through mechanical method from graphite in 2004. It is the basic structural element of many allotrope of carbon, such as graphite and CNTs. This unique two-dimensional carbon material,

which can stably exist, has various novel properties, including high surface area ( $2600 \text{ m}^2 \text{ g}^{-1}$ ), electronic mobility, highest intrinsic mechanical strength and thermal conductivity. <sup>[76]</sup> Based on its impressively high conductivity and surface-to-volume ratio, graphene has been applied in research of LIBs.

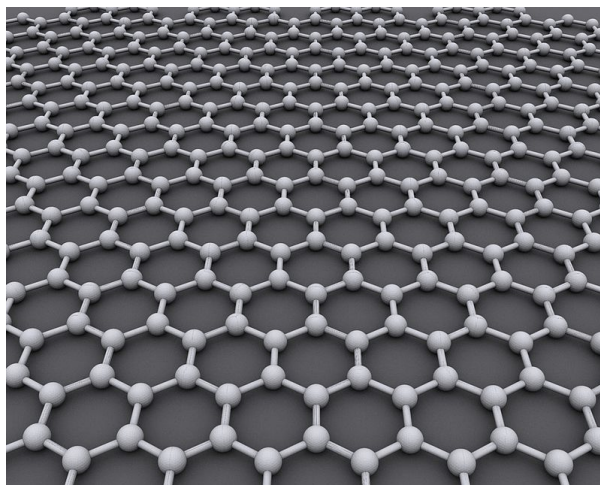


Figure 1.7 Schematic diagram of graphene.

It has been discussed that most of the high-capacity carbon materials can be ascribed to have many available sites for lithium insertion, including (1) each side of the graphene sheet providing the majority of the positions, (2) hydrogen atom terminated edge of the graphene sheet, (3) “covalent” sites and (4) “cavities” of the material. <sup>[77]</sup>

Lithium can be absorbed in both sides of graphene sheet forming a “hamburger” with two layers of lithium as bread and one layer of graphene sheet as meat. The formation of  $\text{Li}_2\text{C}_6$  corresponds to the theoretical capacity of  $744 \text{ mAh g}^{-1}$  for graphene.

It is known to all that the performance of nanomaterials is highly related to their morphology and nanostructure. As a 2D materials, graphene can show good electrochemical properties when existing in form of sheets with fewer layer. <sup>[78-79]</sup>

According to density of states calculation, graphene sheets with 0.7 nm thickness are confirmed to provide highest lithium storage. <sup>[80]</sup> A lot of researches about graphene nanosheets as anode materials for LIB have been published. For example, Lian et al. prepared graphene nanosheets with fewer layers and large surface area by thermally exfoliating the graphene oxide. <sup>[81]</sup> This kind of graphene shows reversible specific capacity reaching 936 mAh g<sup>-1</sup>, 718 mAh g<sup>-1</sup> and 445 mAh g<sup>-1</sup> at current densities of 300 mA g<sup>-1</sup>, 500 mA g<sup>-1</sup> and 1000 mA g<sup>-1</sup> respectively. Wu et al. synthesized N-doped and B-doped graphene nanosheets with reversible capacity of ~500 mAh g<sup>-1</sup> at current density of 0.5 A g<sup>-1</sup>. <sup>[82]</sup> Moreover, the doped graphene can be tolerant of 25 A g<sup>-1</sup>, which is significantly high current density for fast charge.

Nowadays, there have been many mature fabrication methods of graphene in chemical research area or industry. <sup>[83-88]</sup> The most direct way is exfoliation of graphite to obtain graphene with relatively less defect. However, this method is often limited by the size and thickness of graphite. <sup>[89-92]</sup> Another way is using chemical vapor deposition (CVD) with metallic catalysis, including Ni and MgO. This method can produce graphene with several layers and high quality. <sup>[93-94]</sup> The most common way, which is also widely used in commercial fabrication industry, is liquid phase exfoliation from graphite oxide to produce graphene oxide intermediate, followed by reduction. <sup>[95-98]</sup> But the graphene synthesized through this method cannot be fully reduced and the remained oxygen functionalities can have bad impact on graphene's 2D structure with high conductivity. Although this kind of two-dimensional material can exist stably and have many ideal properties, it is found that graphene sheets are easy to stack together. <sup>[99]</sup> Therefore, the complete realization of the theoretical advantages of graphene is prevented by the

combination of defects and thickness caused by multilayer. <sup>[100]</sup> To overcome this drawback, the design of three-dimensional graphene has been reported by many researchers. <sup>[101-104]</sup> With this structure, graphene cannot restack again and can fully realize the ideal properties of graphene.

## 1.6 Ideas in this thesis

There are mainly two designs focused on composites of graphene and SnO<sub>2</sub> nanoparticles in this paper. These ideas are based on the consideration of high electrical conductivity and outstanding mechanical flexibility of graphene and relatively high theoretical capacity of SnO<sub>2</sub>. The first one is an improvement of synthesis method for graphene, prepared by exfoliation of slightly oxidized of graphite. By introducing carboxyl groups on the edge of graphite and using its lower basal plane reactivity than that of the edge, destruction of the conjugation state can be decreased with good dispersion stability. The highly dispersible edge-selectively oxidized graphene obtained contains several layers and is called EOG in the following content. Then SnO<sub>2</sub> nanoparticles with uniform dimension are synthesized onto the surface of EOG through hydrothermal method. The second one is a novel design of three-dimensional graphene, produced by chemical vapor deposition (CVD) with MgO catalysis. The 3D graphene is called flower-like graphene tube (FGT) because of its tube-like architecture composed of layer structure. The SnO<sub>2</sub>-FGT nanocomposites are also synthesized through hydrothermal method. The 3D graphene, FGT, is believed to provide a good conducting network and stable frame for the whole electrode materials.

These materials are then characterized by technologies, including X-ray diffraction, SEM and TEM. In addition, the electrochemical performance of these materials, such as cycling performance, rate capacity and impedance, is tested as electrode materials in lithium ion batteries.

## 2 Experiment

### 2.1 Chemicals

Table 2-1 Table of chemicals.

Name	Molecular Formula	Purity	Manufacturer
Commercial graphite	C		
Sulfuric acid	H <sub>2</sub> SO <sub>4</sub>		Sigma-Aldrich Chemistry
Potassium permanganate	KMnO <sub>4</sub>	99.0%	Sigma-Aldrich Chemistry
Hydrogen peroxide	H <sub>2</sub> O <sub>2</sub>	30%wt	Sigma-Aldrich Chemistry
Ferric chloride	FeCl <sub>3</sub>	97%	Sigma-Aldrich Chemistry
Potassium stannate trihydrate	K <sub>2</sub> SnO <sub>3</sub> •3H <sub>2</sub> O	99.9%	Sigma-Aldrich Chemistry
Magnesium chloride hexahydrate	MgCl <sub>2</sub> •6H <sub>2</sub> O	100.1%	EMD Millipore Corp.
Ammonium bicarbonate	NH <sub>4</sub> HCO <sub>3</sub>	99%	Ridel-de Haën
Acetonitrile	CH <sub>3</sub> CN	99.8%	Sigma-Aldrich Chemistry
Tin(IV) chloride	SnCl <sub>4</sub>	98%	Sigma-Aldrich Chemistry
Sodium hydroxide	NaOH	98.9%	Fisher Chemical

## 2.2 Instruments

Table 2-2 Table of instruments.

<b>Name</b>	<b>Manufacturer</b>
Magnetic stirrer (C-MAG HS 7)	IKA
Analytical balance (College B154)	Mettler TOLEDO
Analytical balance (XS205 DualRange)	Mettler TOLEDO
Stainless steel reaction kettle with Teflon vessel	
Ultrasonic cleaner (2200)	Branson
Laboratory oven (Oven F Air 2.3 CF)	VWR
Tube furnace	MTI Corporation
Glove box & Controlled atmosphere systems	Vacuum Atmospheres Co.
Desktop X-ray diffractometer (MiniFlex II)	Rigaku
Scanning electron microscope (SEM)	
Transmission electron microscope (TEM)	
Battery test system (LANHE)	Wuhan LAND electronics Co., Ltd

## 2.3 Experiments

### 2.3.1 EOG-based SnO<sub>2</sub> materials

#### 1. Synthesis of EOG

The synthesis process of EOG is divided into 3 steps: edge-oxidation of graphite, intercalation of FeCl<sub>3</sub> into edge-oxidized graphite and exfoliation of edge-oxidized graphite using H<sub>2</sub>O<sub>2</sub>.

Firstly, the edge-oxidation reaction was placed in an ice-water bath with temperature under 20 °C. 2 g graphite and 40 ml concentrated H<sub>2</sub>SO<sub>4</sub> were added into a 400 ml container and kept stirring for 30 min. Then 2 g KMnO<sub>4</sub> was added slowly into the reaction solution within 30 min. After 2 more hours, 20 ml distilled water was added and the solution was kept stirring for another 2 h. The final step was adding 2 ml H<sub>2</sub>O<sub>2</sub> and keeping reaction for 30 min. The products, edge-oxidized graphite, were filtered, washed with distilled water and freeze dried.

The second step to prepare FeCl<sub>3</sub> intercalated edge-oxidized graphite was a solid-state reaction. 80 mg as-synthesized edge-oxidized graphite and 400 mg FeCl<sub>3</sub> were milled and mixed together in the environment of inactive gas. Then the mix was transferred and sealed in a stainless still reaction kettle. The kettle was kept in the tube furnace at 600 °C for 6 h with flow of inactive gas. After the kettle cooled down naturally, the products, FeCl<sub>3</sub> intercalated edge-oxidized graphite, were removed from the kettle.

The final step to obtain exfoliated edge-oxidized graphene was by adding 100 mg as-prepared FeCl<sub>3</sub> intercalated edge-oxidized graphite into a H<sub>2</sub>O<sub>2</sub> solution containing 30 ml 30%wt H<sub>2</sub>O<sub>2</sub> and 150 ml distilled water. 200 ml 1M HCl was added into the solution



when no more air bubble was formed in the solution. The final products were washed with distilled water by centrifugation for several times and freeze dried.

## 2. Hydrothermal synthesis of SnO<sub>2</sub> nanoparticles

1.0 g K<sub>2</sub>SnO<sub>3</sub>•3H<sub>2</sub>O was added to 50 ml distilled water, followed by stirring until dissolution. Then the solution was transferred and sealed in 100 ml Teflon vessel with stainless steel reaction kettle. The kettle was kept in laboratory oven at 180 °C for 4 h. After the kettle cooled down naturally, the as-synthesized products were washed with distilled water and ethanol for few times by centrifugation to remove K<sup>+</sup>. The products were finally dried in oven at 60 °C for 8h.

## 3. Hydrothermal synthesis of SnO<sub>2</sub>/EOG nanocomposites

The hydrothermal synthesis method is the same as the above part, except 50 mg EOG was added in the 50 ml solution followed by ultrasonic treatment until uniformly dispersed.

### 2.3.2 FGT-based SnO<sub>2</sub> materials

#### 1. Synthesis of FGT

Since the synthesis method of FGT is based on model sacrifice, we firstly produced MgO model through 3 independent steps.

The first step was to prepare precursor MgCO<sub>3</sub>•3H<sub>2</sub>O with uniform rod structure by precipitation from soluble magnesium salt and bicarbonate salt. So we added 0.04 mol MgCl<sub>2</sub>•6H<sub>2</sub>O and 0.08 mol NH<sub>4</sub>HCO<sub>3</sub> into 60 ml distilled water and stirred the solution until dissolved. Then the solution was transferred into a 100 ml volumetric flask and

diluted with water. A 250 ml round-bottomed flask with 25 ml ethanol stirring at speed of 450 r/min inside was kept in a 50 °C water bath. 50 ml as-prepared solution was added in to the stirring ethanol and kept stirring for 2.5 min. After that, the solution was aged in the 50 °C water bath without stirring for 2 h followed by filtered and washed with water and ethanol. The products were dried in oven at 60 °C for 8h.

The second step was to obtain tube like  $4\text{MgCO}_3\cdot\text{Mg}(\text{OH})_2\cdot 4\text{H}_2\text{O}$  from  $\text{MgCO}_3\cdot 3\text{H}_2\text{O}$  through phase inversion. 2.0 g  $\text{MgCO}_3\cdot 3\text{H}_2\text{O}$  prepared from the first step was added into 60 ml 80 °C water followed by stirring and ultrasonic treatment until uniformly dispersed. Then the solution was stirred at a speed of 450 r/min for 15 min in an 80 °C water bath. The products were filtered, washed with water and ethanol and dried in oven at 60 °C for 8h.

Finally, the MgO model was produced by calcination of  $4\text{MgCO}_3\cdot\text{Mg}(\text{OH})_2\cdot 4\text{H}_2\text{O}$  at 500 °C for 4 h with heating rate of 4 °C/min. FGT was obtained through catalysis of MgO model with  $\text{CH}_3\text{CN}$  flow at 900 °C for 15 min.

## 2. Hydrothermal synthesis of $\text{SnO}_2@\text{FGT}$

$\text{SnO}_2@\text{FGT}$  was prepared through hydrothermal method. 1 mmol  $\text{SnCl}_4$ , 2 mmol NaOH and 30 mg FGT were added into a 60 ml distilled water and ethanol solution and stirred for 30 min. Then the solution was transferred and sealed in 100 ml Teflon vessel with stainless steel reaction kettle. The kettle was kept in laboratory oven at 160 °C for 12 h. After the kettle cooled down naturally, the as-synthesized products were washed with distilled water and ethanol for few times by filtration to remove  $\text{Na}^+$ . The products were finally dried in oven at 60 °C for 8h.

## 2.4 Materials characterization and electrochemical performance tests

### 2.4.1 Materials characterization

#### 1. X-ray Diffraction (XRD)

Powder XRD patterns were obtained from a Rigaku X-ray diffractometer machine using Cu radiation target ( $\lambda = 0.15406$  nm) in reflection geometry at operating voltage of 40 kV and a current of 40 mA. XRD patterns were recorded at a scanning rate of 0.5 deg s<sup>-1</sup> in the  $2\theta$  range from 5 to 90.

#### 2. Raman Scattering Measurement

Raman scattering measurements were obtained by backscattering geometry with a SPEX-1403 laser Raman spectrometer. The excitation source was an argon-ion laser operating at a wavelength of 514.5 nm in the backscattering configuration and a low incident power to avoid thermal effects.

#### 3. Scanning Electron Microscope (SEM)

Some of the powder samples were directly stuck on the conductive tape, while some of the samples were firstly dispersed in ethanol and the solutions were dropped on the Si films, which were stuck on the conductive tape, waiting until the ethanol was fully evaporated. The dropping and evaporation steps were repeated until enough samples were deposited on the Si films.

#### 4. Transmission Electron Microscope (TEM)

All the powder samples were dispersed in ethanol the solutions were dropped on the Cu net waiting until the ethanol was fully evaporated. The dropping and evaporation steps were repeated until enough samples were deposited on the Cu net.

## 2.4.2 Electrochemical performance tests

### 1. Assembly of half cell

The half-cell used for electrochemical testing was made of two electrodes, one using lithium metal as the counter and reference electrode, another using active materials as working electrode. The working electrode was prepared by coating the slurry composed of active powder materials, carbon black and PVDF in a weight ratio of 7:2:1 on a copper foil and drying in a vacuum oven at 90 °C for 8h. A porous membrane was used as a separator. The electrolyte solution in the half cell is 1 mol/L  $\text{LiPF}_6$  dissolved in ethylene carbonate and dimethyl carbonate mixing in a volume ratio of 1:1. The coin cells were assembled in a VAC glovebox filled with argon, while the content of oxygen was controlled under 0.3 ppm. The assembled coin cells were kept steadily for one night and then applied in electrochemical tests.

### 2. Cycling performance testing

The cycling performance testing was operated on LANHE battery test system. The testing conditions to be set included charge/discharge current, voltage range (0.01-3 V) and cycle number. All the tests were performed at room temperature and charged or discharged under constant current density.

### 3. Rate capacity testing

The rate capacity testing was operated on LANHE battery test system. The testing conditions to be set included charge/discharge current, voltage range (0.01-3 V) and cycle number. All the tests were performed at room temperature and charged or discharged under different current densities.

## 3 Results and Discussion

### 3.1 EOG-based SnO<sub>2</sub> materials

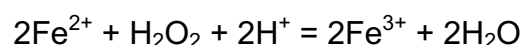
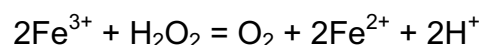
#### 3.1.1 Characterization and electrochemical tests of EOG

The synthesis methods for EOG mainly contains three steps as shown in Figure 3.1.

Firstly, H<sub>2</sub>SO<sub>4</sub> and KMnO<sub>4</sub> are used to oxidize the edges of the graphite, where the purple atoms refer to oxidized carbon atoms. The reason for that is when the graphite contacts with oxidizer, the oxidation reaction always occurs from the periphery.

Therefore, we can control the depth of the oxidation by fixing the concentration of oxidizer to produce the edge-oxidized graphite as we want. Once the graphite is edge-oxidized, it opens tunnels on the surface vertical to the graphene sheets, making it more convenient for FeCl<sub>3</sub> to intercalate as the second step, compared to the bulk graphite.

The FeCl<sub>3</sub> intercalation step is a preliminary expansion process for graphite, producing more spaces between graphene sheets. After adding H<sub>2</sub>O<sub>2</sub> into the mixing solution, H<sub>2</sub>O<sub>2</sub> infiltrates into the spaces provided by FeCl<sub>3</sub> and starts generating oxygen with FeCl<sub>3</sub> as catalyst undergoing the following reactions:



The continuously generating oxygen bubbles can result in the separation of graphene sheets. After repeating several times, single graphene sheets are able to be successfully exfoliated from the bulk graphite. These explanations of our preparation method can be explained by the following characterization results.

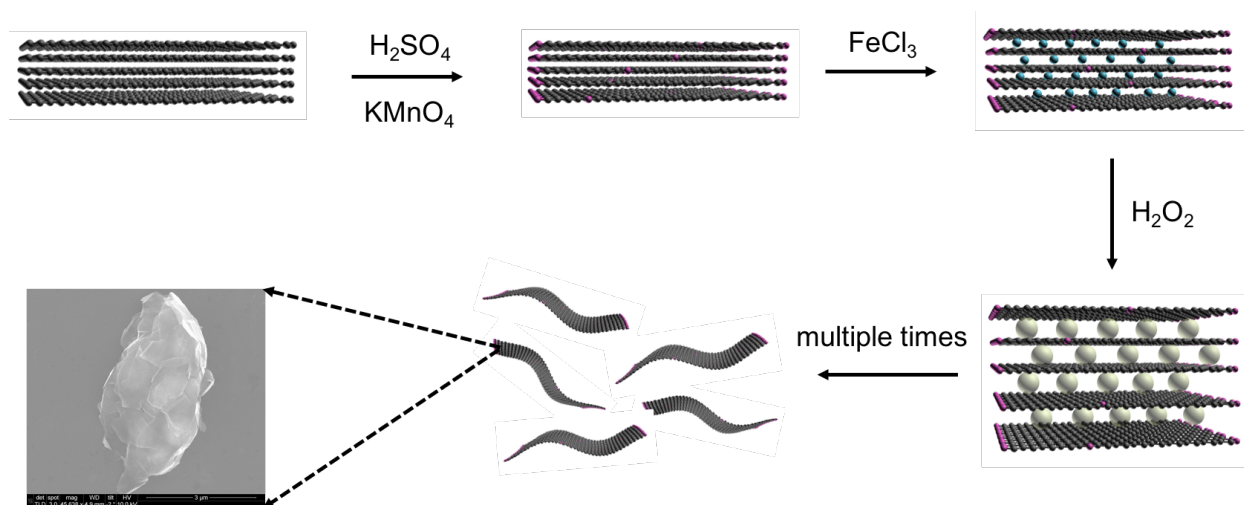


Figure 3.1 Schematic for synthesis process of EOG.

In Figure 3.2 (a), the XRD pattern for graphite shows a characteristic sharp peak at  $2\theta = 26.7^\circ$ . For edge oxidized graphite, except the graphitic peak at  $2\theta = 26.7^\circ$ , another peak at  $2\theta = 10.3^\circ$  illustrates the introduction of oxygen functionalities. The existence of both graphitic and graphene oxides peaks confirms that the oxidation only occurs to part of the graphite. In addition, the oxidation always happens from the outer to the inner. Moreover, the SEM image for edge oxidized graphite (Figure 3.2 (c)) shows rough surface and some hollow spaces, compared with smooth and compact surface of graphite (Figure 3.2 (b)). Hence, the partly oxidized graphite is believed to be edge oxidized graphite. The XRD pattern for  $\text{FeCl}_3$  intercalated edge oxidized graphite shows diffraction peaks for several compounds containing Fe(III), including  $\text{FeCl}_3$ ,  $\text{FeOCl}$  and  $\text{Fe}_2\text{O}_3$ . The obvious layered structure shown in Figure 3.2 (d) indicates that the spaces between graphene sheets have been opened but graphene sheets have not been fully separated yet. These results demonstrate that Fe(III) has successfully intercalated into the graphite, which serves as an important role of catalyst for  $\text{H}_2\text{O}_2$ . Other solid

impurities can be washed by HCl. Figure 3.2 (e) is the SEM image of edge oxidized graphite after being exfoliated for the first time. Compared with Figure 3.2 (d), the smooth graphene sheets are more clearly and the spaces between graphene sheets are expanded. These changes verify the effect of oxygen bubbles generating by  $H_2O_2$  in the exfoliation process.

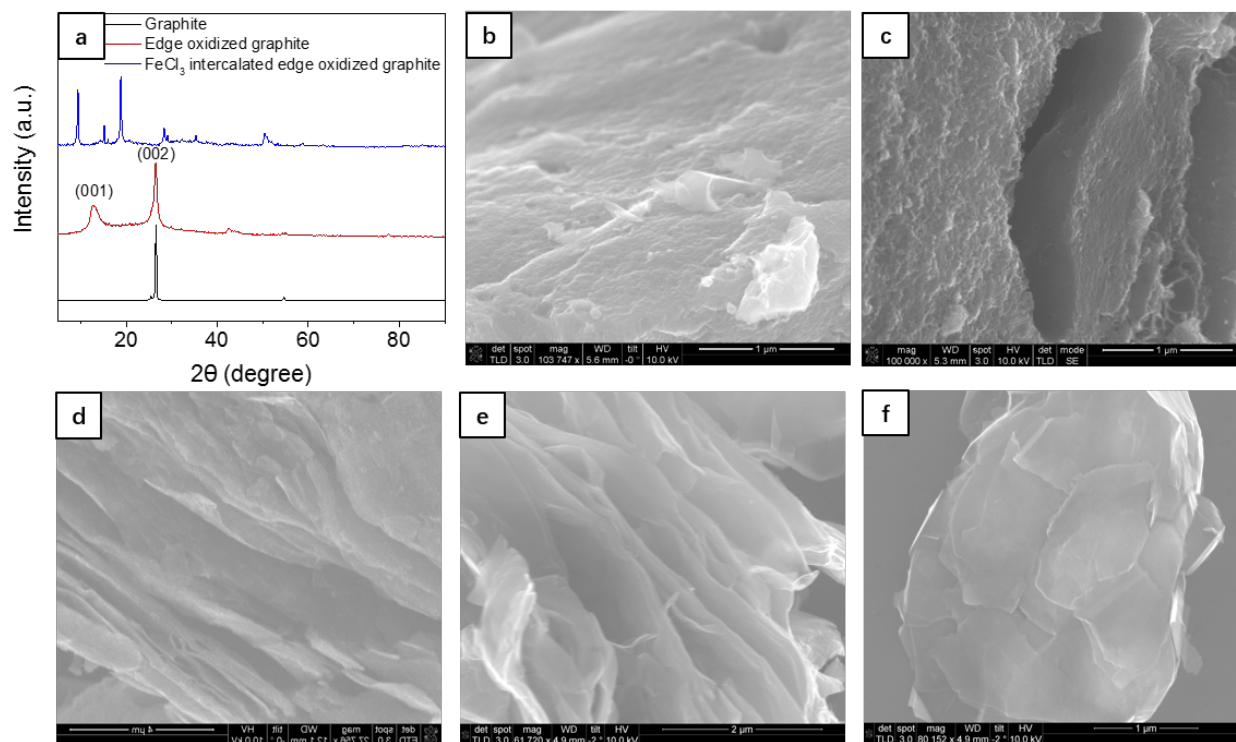


Figure 3.2 (a) XRD pattern of graphite, edge oxidized graphite and  $FeCl_3$  intercalated edge oxidized graphite. SEM images of (b) graphite, (c) edge oxidized graphite, (d)  $FeCl_3$  intercalated edge oxidized graphite, (e)  $FeCl_3$  intercalated edge oxidized graphite exfoliated by  $H_2O_2$  for the first time and (f) single edge oxidized graphene (EOG) sheet.

Figure 3.3 shows the changes of XRD patterns from graphite to graphene during the chemical processing. The peak at  $2\theta = 26.7^\circ$  is a characteristic peak (002) for graphitic



structure, which can be observed in all of these three XRD patterns. Another peak at  $2\theta = 10.3^\circ$ , which refers to (001) diffraction of oxygen functionalities, appearing in edge oxidized graphite becomes quite weak in EOG, suggesting that graphene sheets have been successfully exfoliated and the oxygen functionalities present a much smaller part in EOG than edge oxidized graphite. Moreover, most of the graphene produced by researchers shows a flat peak at  $2\theta = 26.7^\circ$ , while the peak for EOG is extremely sharp. This comparison demonstrates high crystalline structure of EOG.

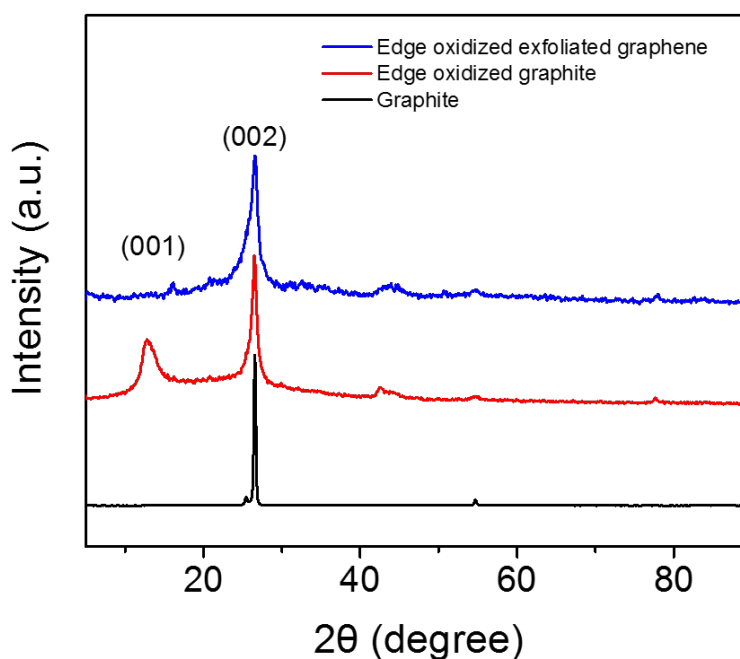


Figure 3.3 XRD patterns of graphite, edge oxidized graphite and edge oxidized exfoliated graphene.

Raman spectroscopy is an effective approach to characterize graphitic materials, especially when used to determine ordered and disordered crystal structure in graphene. Figure 3.4 presents the significant structural changes during the synthesis process from graphite to graphene. All of these three Raman spectra have two obvious

peaks at  $\sim 1580\text{ cm}^{-1}$  and  $\sim 2700\text{ cm}^{-1}$ , which are called G-band and 2D band respectively. G-band arises from the stretching motion of C-C bond in graphitic materials, which is common to all  $\text{sp}^2$  carbon systems. <sup>[105]</sup> 2D band is a second-order two-phonon process and exhibits a strong frequency dependence on the excitation laser energy. The presence of both G-band and 2D band is a characteristic Raman spectrum for graphitic materials. The most distinguished difference among these three spectra is the relative strength of D-band at  $\sim 1350\text{ cm}^{-1}$ , which is a disorder-induced band. In Raman spectrum for graphite, D-band is very weak and almost forbidden, corresponding to high-crystalline structure in graphite. A significant rise in D-band of edge part of exfoliated graphene suggests a large part of disorder carbon structure in this area, referring to oxygen functionalities producing  $\text{sp}^3$  domains. Compared with D/G ratio of graphite, that of central part of exfoliated graphene shows a great increase, indicating the decrease of the size of the in-plane  $\text{sp}^2$  domains. However, when compared with D/G ratio of edge part of exfoliated graphene, the notable decrease in that of central part, related to less  $\text{sp}^3$  domains, confirms that only edge part of exfoliated graphene is oxidized.

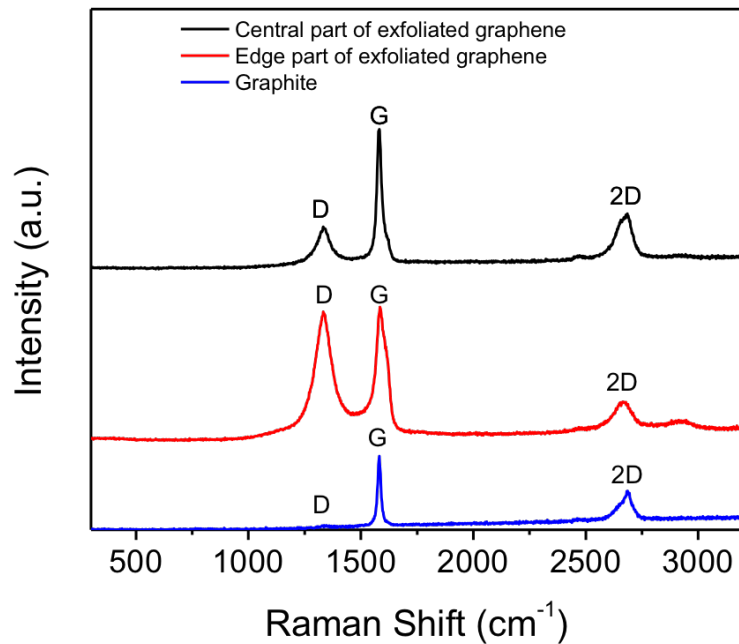


Figure 3.4 Raman spectra of graphite, edge part of exfoliated graphene and central part of exfoliated graphene.

From the SEM and TEM images of EOG in Figure 3.5 (a-c), we can find that the graphene sheet is quite thin and has a large surface area. The average dimension of a single EOG is around 1-2  $\mu\text{m}$ . The crystal lines shown in EOG's HRTEM image (Figure 3.5 (d)) illustrates that the EOG has good crystalline structure, which supports that the EOG is graphene according to its definition.

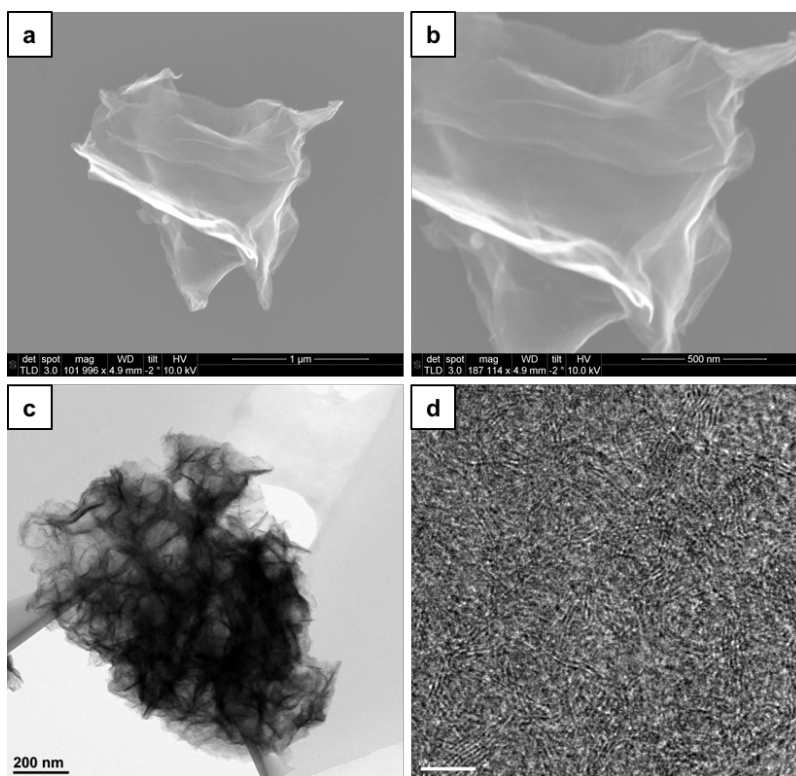


Figure 3.5 (a) (b) SEM images of EOG with different scalar of 1  $\mu\text{m}$  and 500 nm respectively. (c) TEM image of EOG. (d) HRTEM image of EOG.

Cycle performance of EOG at different current densities from 0.1  $\text{A g}^{-1}$  to 1  $\text{A g}^{-1}$  is shown in Figure 3.6. The reversible capacity of EOG electrode is around 650  $\text{mAh g}^{-1}$  at 0.1  $\text{A g}^{-1}$ , 380  $\text{mAh g}^{-1}$  at 0.3  $\text{A g}^{-1}$ , 200  $\text{mAh g}^{-1}$  at 0.5  $\text{A g}^{-1}$  and 150  $\text{mAh g}^{-1}$  at 1  $\text{A g}^{-1}$ . After 40 cycles of rate capacity test, the capacity of EOG electrode can be still remained at 420  $\text{mAh g}^{-1}$  at 0.1  $\text{A g}^{-1}$ , which is higher than the capacity of commercial carbon anode. These electrochemical test results illustrate that EOG with fewer layers can be a candidate of anode material for lithium ion batteries due to its stable cycle performance and relatively high reversible capacity.

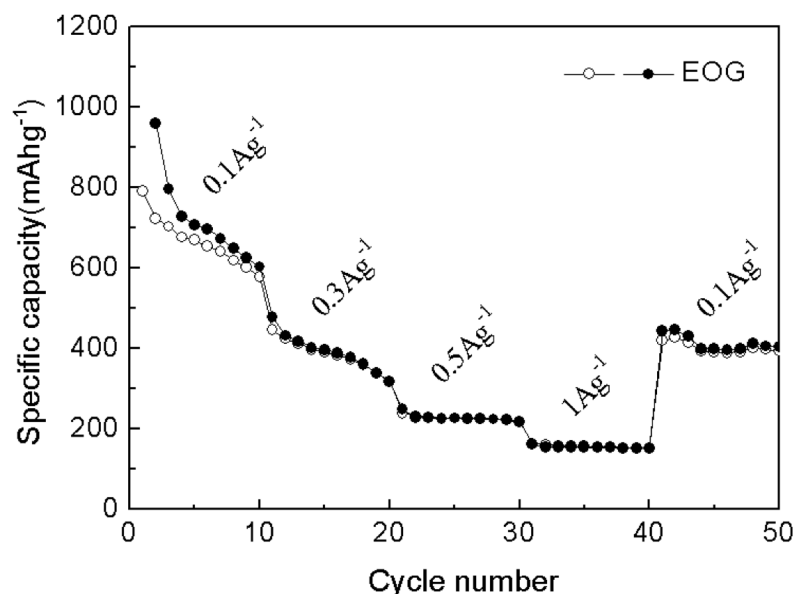


Figure 3.6 Cycle performance of EOG at different current densities from 0.1 A g<sup>-1</sup> to 1 A g<sup>-1</sup>.

### 3.1.2 Characterization and electrochemical test results of SnO<sub>2</sub> nanoparticles and SnO<sub>2</sub>/EOG nanocomposites

Although the test results of reversible capacity of EOG is much higher than that of commercial carbon, it still shows insufficiency when compared with high capacity materials, such as SnO<sub>2</sub>. In contrast, although SnO<sub>2</sub> owns high theoretical capacity, the significant effect of volume expansion limits its use in LIB and leads to degradation after cycling tests. Therefore, SnO<sub>2</sub> nanoparticles are designed to be in-situ grown onto EOG surface to produce SnO<sub>2</sub>/EOG nanocomposites and bare SnO<sub>2</sub> nanoparticles are synthesized as comparison. Figure 3.7 shows the schematic for synthesis process of bare SnO<sub>2</sub> nanoparticles and SnO<sub>2</sub>/EOG nanocomposites. The only different step is that EOGs are firstly dispersed into the solution.

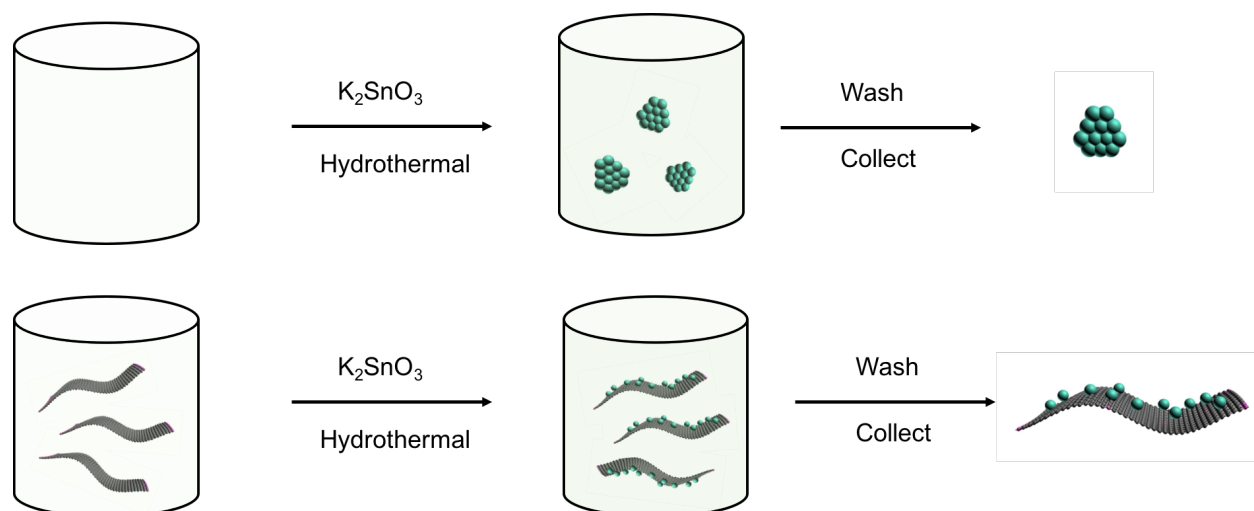


Figure 3.7 Schematic for synthesis process of bare SnO<sub>2</sub> nanoparticles and SnO<sub>2</sub>/EOG nanocomposites.

To characterize the materials, XRD is firstly used to confirm the chemical compounds of the products synthesized through hydrothermal method. Figure 3.8 shows the XRD patterns for bare SnO<sub>2</sub> nanoparticles and SnO<sub>2</sub>/EOG nanocomposites. The obvious sharp peaks in both of the XRD patterns are almost overlapped and match well with the standard XRD pattern for tetragonal SnO<sub>2</sub> phase (JCPDS: 71-0652), especially the three strongest peaks corresponding to (110), (101) and (211) crystal planes. Hence, the XRD confirms the composition of our nanoparticles and nanocomposites is SnO<sub>2</sub>.

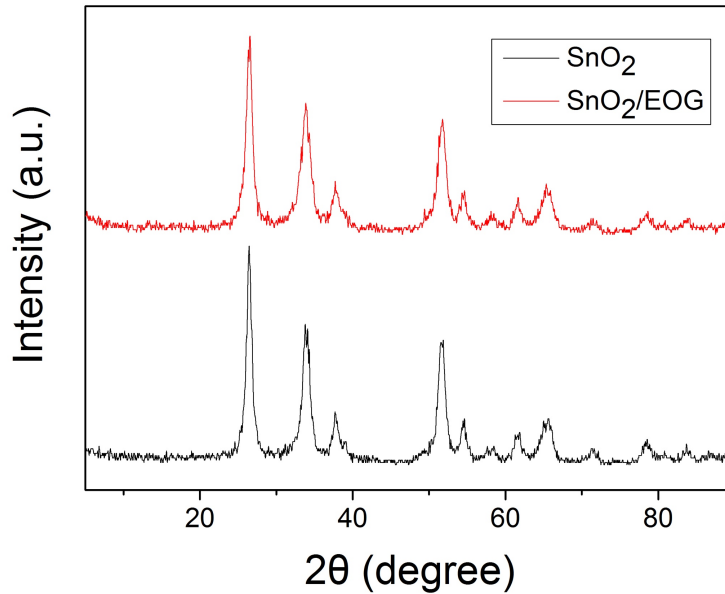


Figure 3.8 XRD patterns of bare SnO<sub>2</sub> nanoparticles and SnO<sub>2</sub>/EOG nanocomposites.

The architecture of bare SnO<sub>2</sub> nanoparticles and SnO<sub>2</sub>/EOG nanocomposites was analyzed by TEM and HRTEM as presented in Figure 3.9. Figure 3.9 (a) shows that bare SnO<sub>2</sub> nanoparticles are clustered together due to their small average dimension around 10 nm, which is observed from Figure 3.9 (b). Figure 3.9 (c) shows a TEM image with low magnification for SnO<sub>2</sub>/EOG nanocomposites suggesting that SnO<sub>2</sub> nanoparticles are uniformly anchored on EOG surface. This structure can be studied more deeply in Figure 3.9 (d), where the darker particles correspond to SnO<sub>2</sub> nanoparticles and the lighter area refers to the graphene sheet. Moreover, the clear crystal lattice with spacing of 0.33 nm shown in both Figure 3.9 (b) and (d) is related to the (110) face of the SnO<sub>2</sub> rutile phase. Therefore, it is certain that SnO<sub>2</sub> nanoparticles in-situ grown on the surface of EOG are well crystallized.

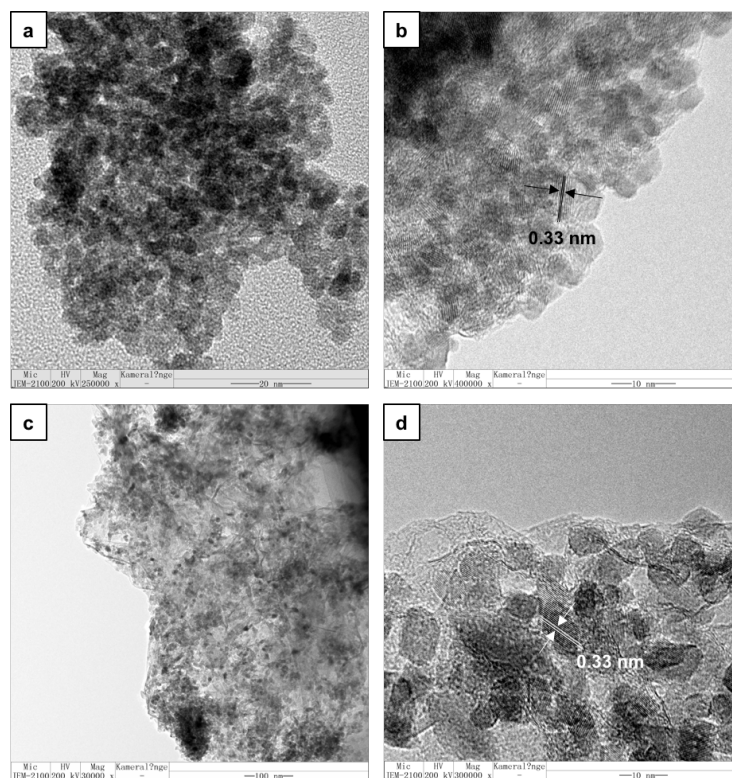


Figure 3.9 (a) TEM image and (b) HRTEM image for SnO<sub>2</sub> nanoparticles. (c) TEM image and (d) HRTEM image for SnO<sub>2</sub>/EOG nanocomposites.

Both bare SnO<sub>2</sub> nanoparticles and SnO<sub>2</sub>/EOG nanocomposites were applied as anode materials in lithium ion batteries for electrochemical tests. For cycling test, they finished 50 cycles of discharge and charge under constant current density of 0.1 A g<sup>-1</sup>. Fig 3.10 presents the discharge/charge profile of the first, second and last cycle. They both exhibit quite different performance in their first and second cycles. For bare SnO<sub>2</sub> nanoparticles, the specific discharge capacity for the first cycle is 1905 mAh g<sup>-1</sup>. But it drops to 1107 mAh g<sup>-1</sup> in the second cycle dramatically. SnO<sub>2</sub>/EOG nanocomposites demonstrate higher initial discharge capacity of 2370 mAh g<sup>-1</sup>. After the first cycle, the discharge capacity of 1495 mAh g<sup>-1</sup> is obtained. The significant irreversible capacity around 800 mAh g<sup>-1</sup> in the first cycle is not only caused by the irreversible reaction from



SnO<sub>2</sub> to Sn according to its mechanism, but also the formation of the solid electrolyte interface (SEI) layer. The relatively higher capacity performed in SnO<sub>2</sub>/EOG nanocomposites can be consumed to the existence of EOG, which increases the electric conductivity in the electrode. After 50 cycles, the discharge/charge profile for bare SnO<sub>2</sub> nanoparticles shows quite huge deviation from the second cycle. Moreover, the discharge and charge capacities of the 50<sup>th</sup> cycle are nearly 35% lower than that of the second cycle. However, for SnO<sub>2</sub>/EOG nanocomposites as shown in Figure 3.10 (b), the discharge/charge curves of the second cycle and the 50<sup>th</sup> cycle are overlapped, suggesting negligible change in the capacity. This result verifies that the addition of EOG to SnO<sub>2</sub> can decrease the effect of volume expansion and stabilize the whole electrode.

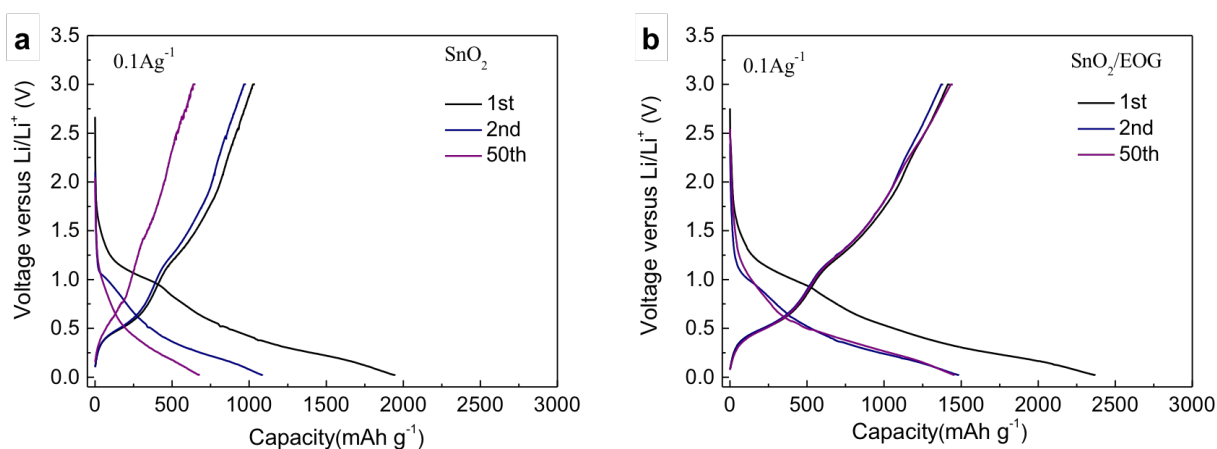


Figure 3.10 Discharge/charge profile of 1<sup>st</sup>, 2<sup>nd</sup> and 50<sup>th</sup> cycle for (a) bare SnO<sub>2</sub> nanoparticles and (b) SnO<sub>2</sub>/EOG nanocomposites.

The complete cycle performance of bare SnO<sub>2</sub> nanoparticles and SnO<sub>2</sub>/EOG nanocomposites is revealed in Figure 3.11. After the second cycle, bare SnO<sub>2</sub> nanoparticles electrode keeps degrading, resulting in the capacity of 687 mAh g<sup>-1</sup> after

50 cycles. However, the cycling capacity for SnO<sub>2</sub>/EOG nanocomposites electrode is remained at around 1500 mAh g<sup>-1</sup>. This result is much higher than bare SnO<sub>2</sub> nanoparticles and shows excellent cycling stability after 50 cycles, evidenced by the flat curve of the cycle performance.

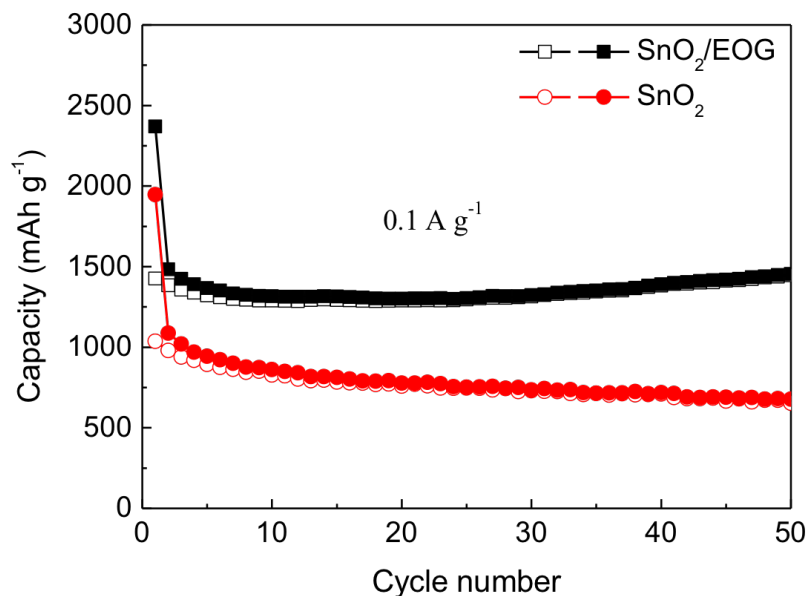


Figure 3.11 Cycle performance of bare SnO<sub>2</sub> nanoparticles and SnO<sub>2</sub>/EOG nanocomposites at constant current density of 0.1 A g<sup>-1</sup>.

The rate performance of bare SnO<sub>2</sub> nanoparticles and SnO<sub>2</sub>/EOG nanocomposites was carried under varied current densities. For bare SnO<sub>2</sub> nanoparticles, the reversible capacity is ~1000 mAh g<sup>-1</sup> at 0.1 A g<sup>-1</sup>, ~750 mAh g<sup>-1</sup> at 0.2 A g<sup>-1</sup>, ~600 mAh g<sup>-1</sup> at 0.5 A g<sup>-1</sup> and ~450 mAh g<sup>-1</sup> at 1 A g<sup>-1</sup>. When the current density reverses back to the initial low value, although the reversible capacity can reach up to almost the original testing result, it still shows obvious fading in the 5 cycles. This performance indicates that bare SnO<sub>2</sub> nanoparticles can handle high current density but still face the problem caused by

degradation. SnO<sub>2</sub>/EOG nanocomposites exhibit high rate performance, where the average capacities are maintained as high as ~1400 mAh g<sup>-1</sup> at 0.1 A g<sup>-1</sup>, ~1200 mAh g<sup>-1</sup> at 0.2 A g<sup>-1</sup>, ~1100 mAh g<sup>-1</sup> at 0.5 A g<sup>-1</sup> and 1000 mAh g<sup>-1</sup> at 1 A g<sup>-1</sup>. Moreover, when the current density drops back to 0.1 A g<sup>-1</sup>, the capacity can recover to the initial value, around 1400 mAh g<sup>-1</sup>. These results confirm that SnO<sub>2</sub>/EOG nanocomposites are tolerant to high current density and high rate cycling.

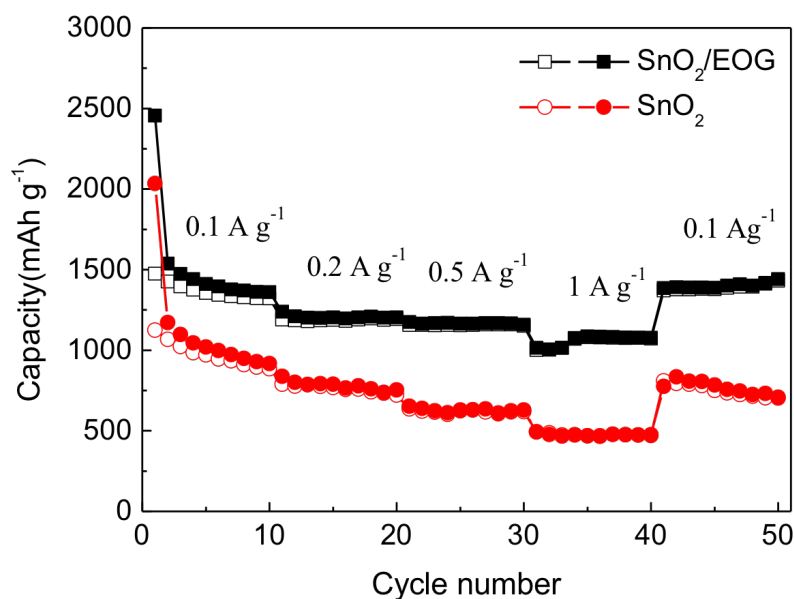


Figure 3.12 Cycle performance of bare SnO<sub>2</sub> nanoparticles and SnO<sub>2</sub>/EOG nanocomposites at different current densities from 0.1 A g<sup>-1</sup> to 1 A g<sup>-1</sup>.

Electrochemical impedance spectroscopy (EIS) is an important testing technology applied in studying electrochemical interface and electrode reaction. Figure 3.13 presents the electrochemical impedance spectra of bare SnO<sub>2</sub> nanoparticles and SnO<sub>2</sub>/EOG nanocomposites. For simplification, both of the spectra are considered to consist of a semicircle and an oblique line. The semicircle refers to chemical reaction

resistance or charge transfer, and the oblique line corresponds to the diffusion of lithium ions in active materials of electrode. In order to confirm the positive effect of the addition of EOG on electric conductivity, we are more focused on the resistance, indicated by the x-intercept. As is shown, the resistance for SnO<sub>2</sub>/EOG nanocomposites (18 Ω) is quite smaller than that of bare SnO<sub>2</sub> nanoparticles (82 Ω), demonstrating that it is much easier for charge transfer between electrolyte and electrode. Therefore, the existence of EOG can efficiently increase the intrinsic electric conductivity.

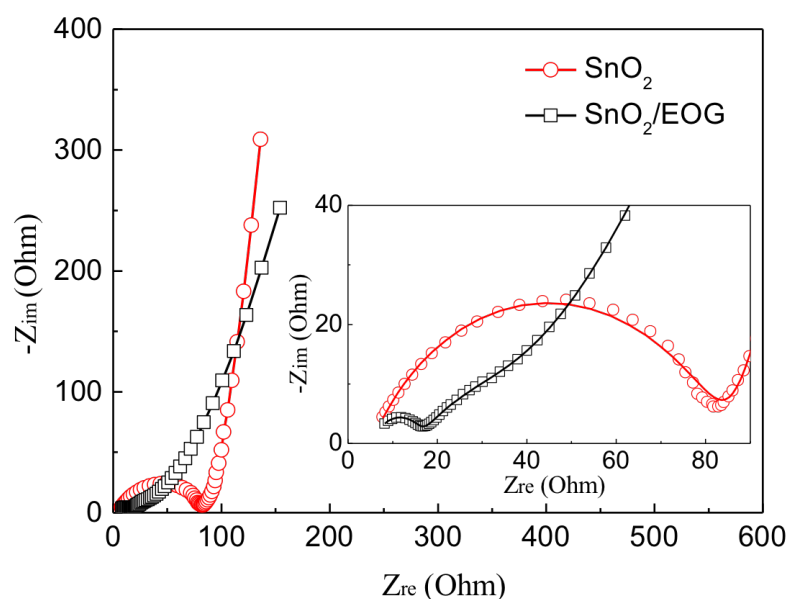
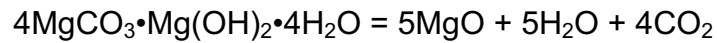
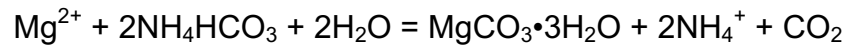


Figure 3.13 Electrochemical impedance spectra of bare SnO<sub>2</sub> nanoparticles and SnO<sub>2</sub>/EOG nanocomposites. The inset part is magnification of the original spectra.

## 3.2 FGT-based SnO<sub>2</sub> nanomaterials

### 3.2.1 Characterization results of FGT

The synthesis process of MgO template is considered into three steps, undergoing the following chemical reactions:



The first step is obtaining MgCO<sub>3</sub>•3H<sub>2</sub>O with rod structure by pyrolysis of Mg(HCO<sub>3</sub>)<sub>2</sub>, which is normally a homogeneous nucleation process, where nucleation and growth are at the same time. But, this process is usually slow and results in irregular morphology and dimension. In order to achieve uniform particles with relatively large dimension, it is accepted to separate the nucleation and growth process by creating conditions for explosive nucleation. Therefore, ethanol is chosen to reduce the solubility, as well as accelerate the nucleation and produce uniform nanoparticles. For the second step, 4MgCO<sub>3</sub>•Mg(OH)<sub>2</sub>•4H<sub>2</sub>O is confirmed to be able to self-assemble layer structure. Hence, in this paper, flower-like 4MgCO<sub>3</sub>•Mg(OH)<sub>2</sub>•4H<sub>2</sub>O tube is designed to be self-assembled from 4MgCO<sub>3</sub>•Mg(OH)<sub>2</sub>•4H<sub>2</sub>O nanosheets, which look like petals. Finally, the flower-like tube structure of MgO template is maintained by direct calcination.

The remaining synthesis steps for flower-like graphene tube (FGT) contains CVD catalysis with acetonitrile and etching the template with HCl as shown in Figure 3.14.

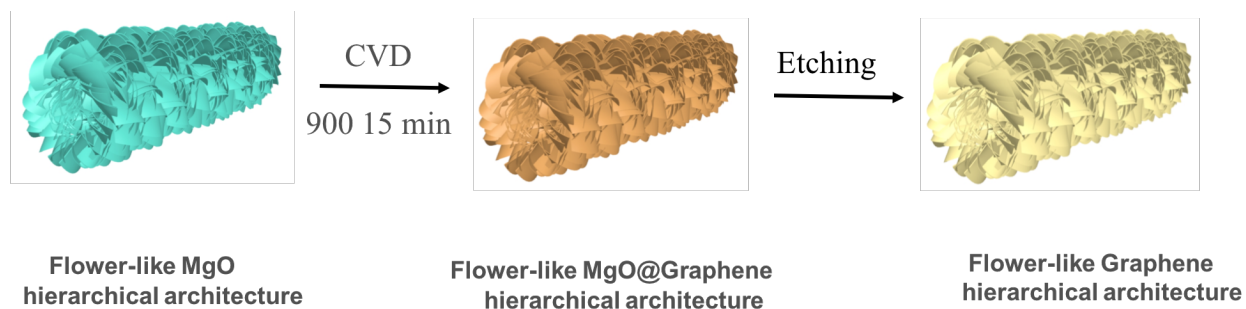


Figure 3.14 Schematic for synthesis process of flower-like graphene tube (FGT) from flower-like MgO tube template.

The following characterization results are mainly focused on flower-like MgO tube template, MgO@graphene intermediate and flower-like graphene tube (FGT). As shown in Figure 3.15, the peaks in XRD pattern for MgO template correspond to MgO standard XRD pattern, but they are weak and flat. Once the MgO template has been catalyzed under high temperature, the peaks in XRD pattern for MgO@graphene intermediate becomes sharp and strong, demonstrating that the crystal structure of MgO template has been improved. In the XRD pattern for FGT, the peaks for MgO disappear, illustrating that the MgO model has been etched. The wide and flat peak refers to graphene produced by catalysis of MgO template.

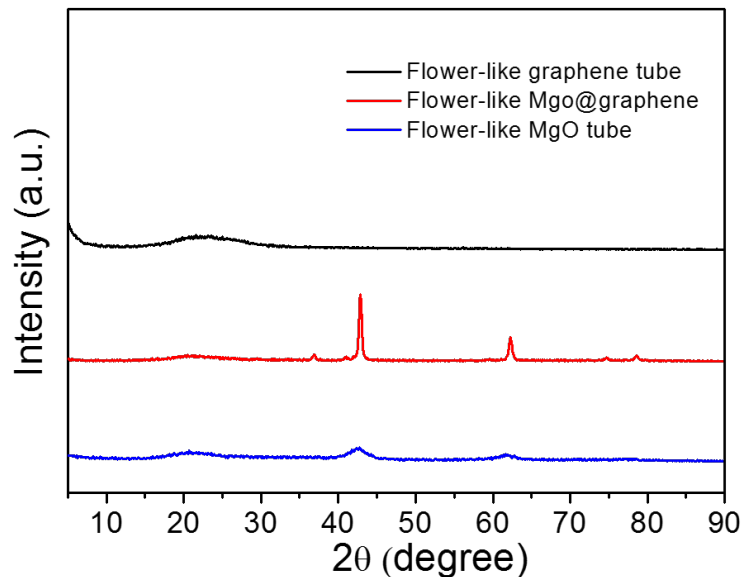


Figure 3.15 XRD pattern for flower-like MgO tube, flower-like MgO@graphene and flower-like graphene tube (FGT).

The microstructure and architecture of flower-like MgO tube template, MgO@graphene intermediate and FGT are studied by SEM and SEM mapping. Figure 3.16 refers to the morphology of MgO template by SEM in the magnification of 50  $\mu\text{m}$  and element distribution of magnesium and oxygen by SEM mapping. From Figure 3.16 (a), MgO templates are shown as tube structure and their dimension is quite uniform with width of  $\sim 10 \mu\text{m}$  and length of  $\sim 40 \mu\text{m}$ . The microstructure of MgO template can be clearly observed from Figure 3.16 (b). The shell of the MgO tube is composed of many nanosheets like petals arranged in random directions, which can produce large surface area and good mechanical property. In order to take a deep look at the element distribution of MgO template, SEM mapping is used to scan magnesium and oxygen in

the chosen sample. The results shown in Figure 3.16 (c) and (d) indicate that magnesium and oxygen are distributed uniformly among the specific MgO sample.

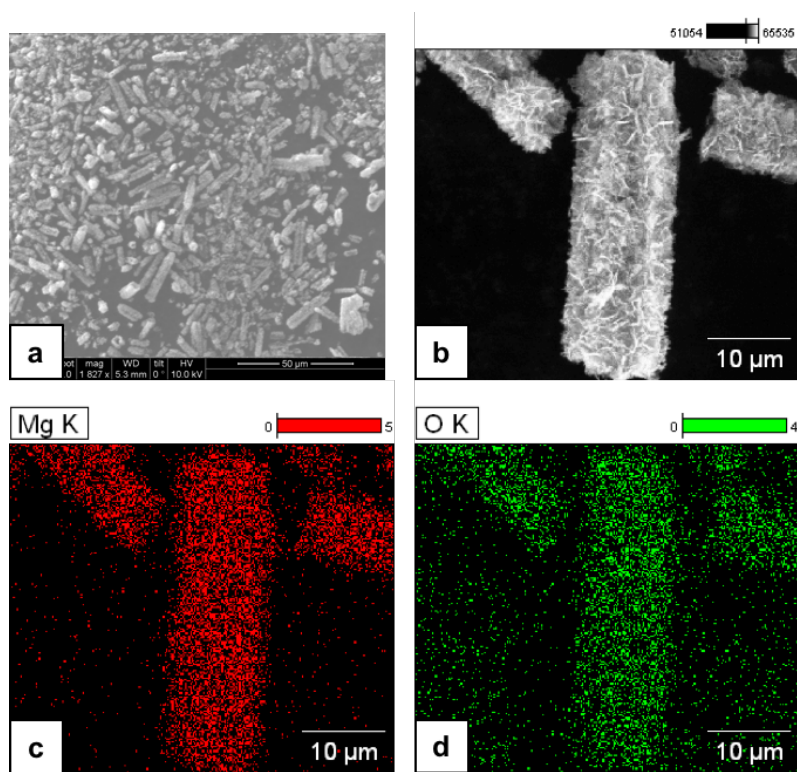


Figure 3.16 (a) SEM image for flower-like MgO hierarchical tube. (b-d) SEM mapping for flower-like MgO hierarchical tube, (c) and (d) respectively refer to the element distribution of magnesium (Mg) and oxygen (O) among the selected sample in (b).

Figure 3.17 shows the SEM image and SEM mapping results for MgO@graphene intermediate. The overall tube structure of the intermediate shown in Figure 3.17 (a) is remained the same as MgO template even after catalysis at high temperature, suggesting the thermal stability of MgO template. Moreover, Figure 3.17 (b) confirms that microstructure of layer structure is also kept in the intermediate. The rest figures in Figure 3.17 refer to the SEM mapping results of magnesium, oxygen, carbon and nitrogen. The distribution of magnesium and oxygen is similar as that of MgO template.



Since the graphene is synthesized from acetonitrile, so the graphene obtained is considered to contain carbon and nitrogen, forming N-doped graphene. Figure 3.17 (e) and (f) confirm the element constitution of carbon and nitrogen in the graphene.

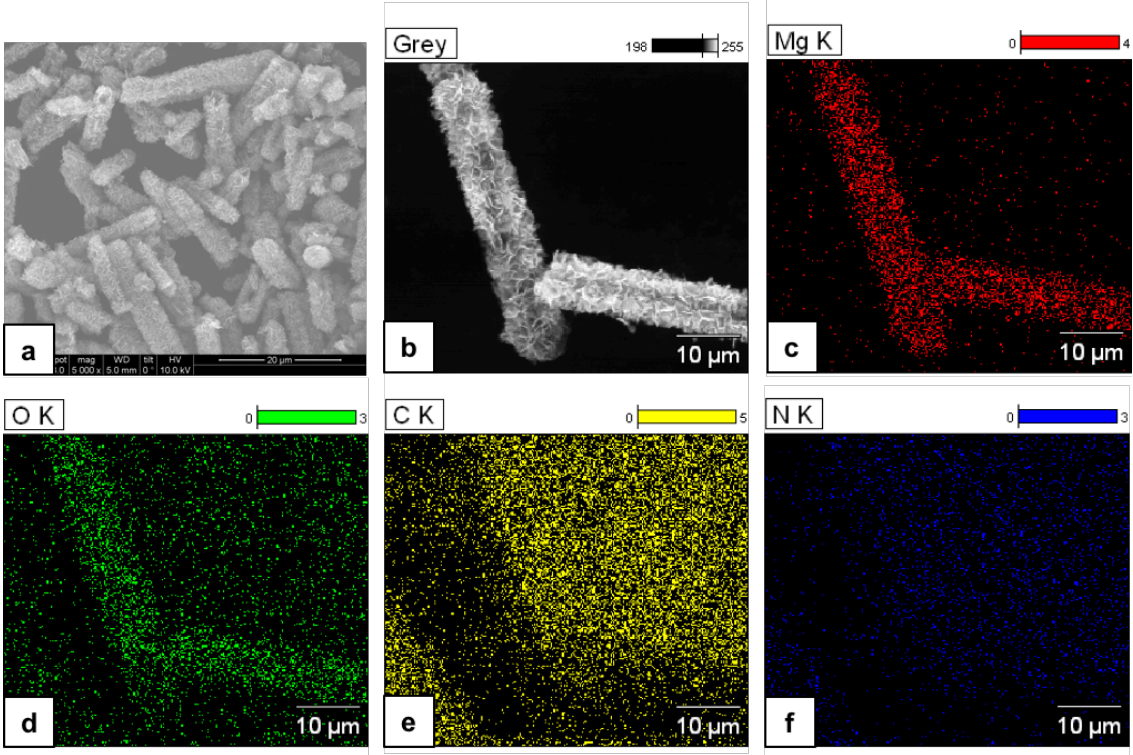


Figure 3.17 (a) SEM image for MgO@graphene intermediate. (b-f) SEM mapping for MgO@graphene intermediate, (c), (d), (e) and (f) respectively refer to the element distribution of magnesium (Mg), oxygen (O), carbon (C) and nitrogen (N) among the selected sample in (b).

After etching, our FGT is designed to keep the layer composed tube structure to produce a three-dimensional graphene. Figure 3.18 presents our FGT in different magnifications, from 20 μm to 2 μm. As is shown in Figure 3.18 (a), the macroscopic structure of FGT looks the same as our MgO template, remaining the same dimension with width of ~10 μm and length of ~40 μm. The microstructure of FGT is also confirmed unchanged from MgO template in Figure 3.18 (d). The clear layer structure produces

high surface area and the three-dimensional architecture prevents graphene sheets from stacking together. When the graphene with this kind of structure is used in lithium ion batteries, it is believed to perform better than those graphene with two-dimensional structure due to conductivity net with high efficiency provided by 3D structure.

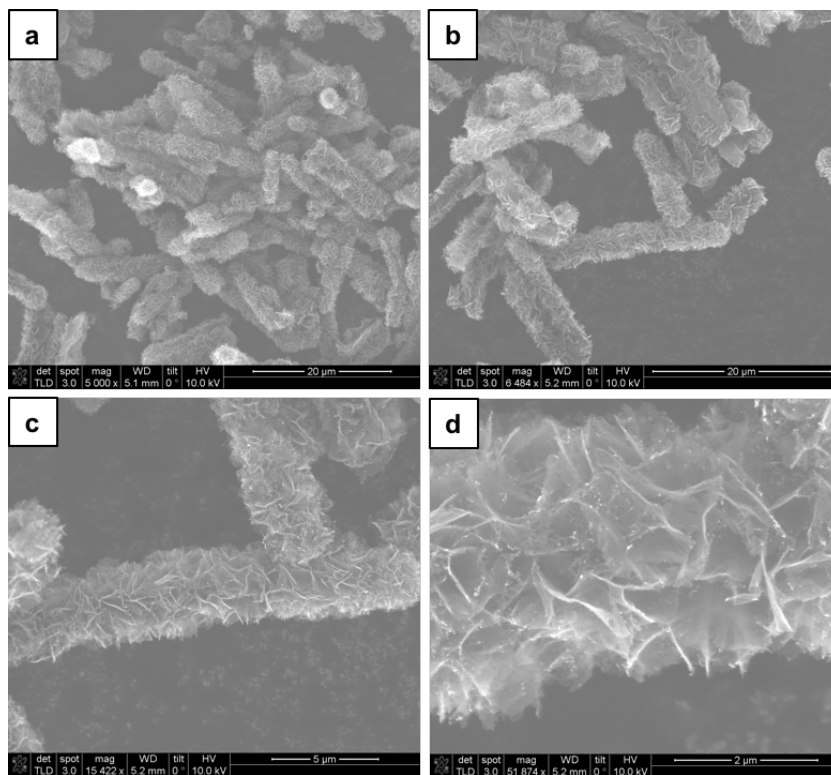


Figure 3.18 SEM images for flower-like graphene tube (FGT) in different magnifications.

### 3.2.2 Characterization and electrochemical test results of SnO<sub>2</sub>-FGT nanocomposites

In order to overcome the drawback of relatively low theoretical capacity of graphene, as well as decrease the effect of volume expansion and insufficient electric conductivity of SnO<sub>2</sub>, SnO<sub>2</sub> is designed to in-situ grow on the surface of our FGT. Figure 3.19 briefly demonstrates the synthesis idea of our SnO<sub>2</sub>-FGT nanocomposites. For simplification, the architecture of the cross section for FGT is displayed like a sunflower, with the circle

simulating the tube structure and petals simulating the layer structure. After hydrothermal synthesis using  $\text{SnCl}_4$ ,  $\text{SnO}_2$  nanoparticles, shown as small blue circles, adhere to the surface of the layer structure of FGT. It is considered that  $\text{SnO}_2$  nanoparticles contacting directly with the 3D conductivity net, produced by FGT, can show higher electric conductivity. In addition, during the discharge and charge process, even if the volume expansion of  $\text{SnO}_2$  may cause pulverization of itself, the 3D structure of FGT can help to collect and reactive the disintegrated active materials. This kind of nanocomposites is studied by the following characterization and electrochemical test results.

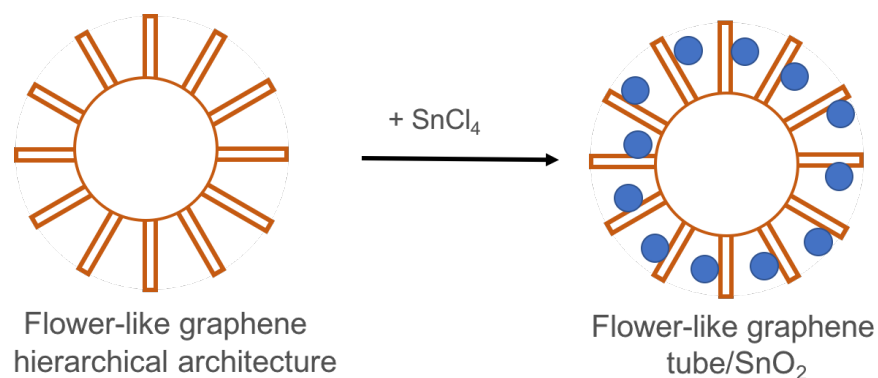


Figure 3.19 Schematic for synthesis process of  $\text{SnO}_2$ -FGT nanocomposites.

XRD is firstly used to confirm the products synthesized through hydrothermal method are  $\text{SnO}_2$ -FGT nanocomposites. The obvious sharp peaks in the XRD pattern (Figure 3.20) match well with the standard XRD pattern for tetragonal  $\text{SnO}_2$  phase (JCPDS: 71-0652), especially the three strongest peaks corresponding to (110), (101) and (211) crystal planes. The weak diffraction peak at around  $2\theta = 20^\circ$  refers to graphene. The slight deviation from  $2\theta = 26.7^\circ$  is highly possibly because of the existence of  $\text{SnO}_2$ .

Hence, the XRD confirms the composition of our nanocomposites is SnO<sub>2</sub> and graphene.

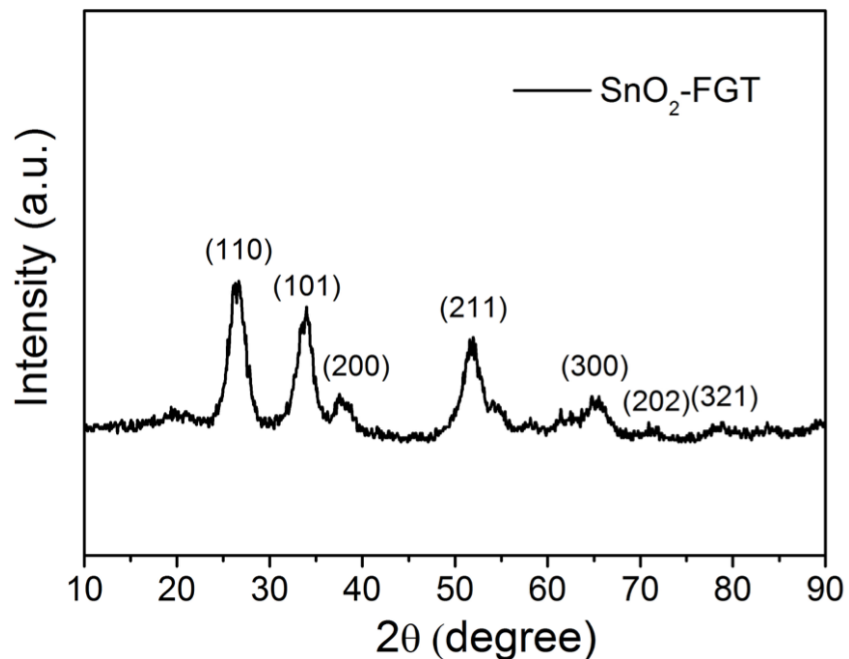


Figure 3.20 XRD pattern for SnO<sub>2</sub>-FGT nanocomposites.

SEM is applied on observation of the microstructure of SnO<sub>2</sub>-FGT nanocomposites. Figure 3.21 (a) shows that the tube structure is kept well even after the hydrothermal synthesis at high temperature and pressure. From the SEM images with higher magnification (Figure 3.21 (c)), non-uniform SnO<sub>2</sub> nanoparticles, marked with a circle as an example, with dimension from several nanometers to tens of nanometers can be found attached to the layer structure of FGT. It can be imagined that during discharge and charge process, SnO<sub>2</sub> nanoparticles with dimension of several nanometers can handle the stress from volume expansion, while SnO<sub>2</sub> nanoparticles with larger size are likely pulverized. Under these circumstances, the randomly arranged layer structure can serve as a collector, remaining the active material as much as possible. The

effectiveness of this structure can be analyzed from the following electrochemical tests, including discharge/charge profile, cycling test and rate capacity test.

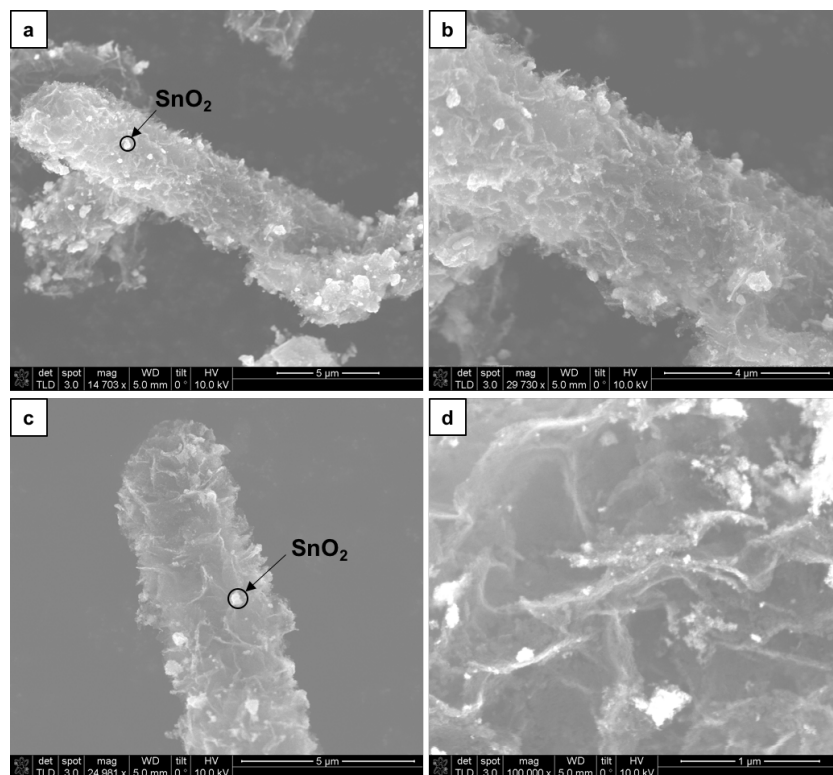


Figure 3.21 SEM images for SnO<sub>2</sub>-FGT nanocomposites in different magnifications.

SnO<sub>2</sub>-FGT nanocomposites are used as anode materials in lithium ion batteries for electrochemical tests. To test the cycling performance of SnO<sub>2</sub>-FGT nanocomposites, current densities of 0.1 A g<sup>-1</sup> and 1 A g<sup>-1</sup> are applied on SnO<sub>2</sub>-FGT nanocomposites electrode during repeated discharge and charge procedure in the voltage window from 0.1 V to 3.0 V. The discharge/charge profile of the first, second and fiftieth cycle under current density of 0.1 A g<sup>-1</sup> is displayed in Figure 3.22. The specific discharge capacity for the first cycle is ~ 2700 mAh g<sup>-1</sup>, but in the second cycle, it drops to ~1650 mAh g<sup>-1</sup> drastically. The reason for this is the same as what we have discussed in SnO<sub>2</sub>/EOG nanocomposites. The irreversible capacity comes from the formation of SEI layer and

the irreversible chemical reaction from SnO<sub>2</sub> to Sn. The curves for the second and fiftieth cycle are nearly overlapped, illustrating that our SnO<sub>2</sub>-FGT nanocomposites keep electrochemically stable during the cycling discharge and charge process.

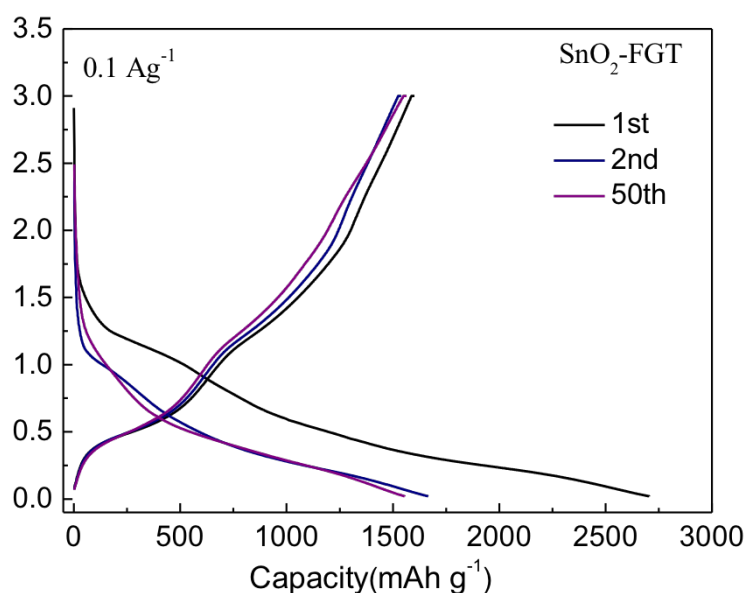


Figure 3.22 Discharge/charge profile of 1<sup>st</sup>, 2<sup>nd</sup> and 50<sup>th</sup> cycle for SnO<sub>2</sub>-FGT nanocomposites.

The complete cycling performance for 50 cycles under current densities of 0.1 A g<sup>-1</sup> and 1 A g<sup>-1</sup> respectively is shown in Figure 3.23. For the first 50 cycles, except the first cycle, the reversible capacities are stabled in the range between ~1300 mAh g<sup>-1</sup> and ~1500 mAh g<sup>-1</sup>. However, the curve still presents a slight decrease and then increase. The reason for the decreasing part is the slow completion process of irreversible reaction and degradation of active materials. After that, the pulverized materials undergo reactivation, resulting in the increase of reversible capacity. When the 50 cycles under current density of 0.1 A g<sup>-1</sup> are finished, the SnO<sub>2</sub>-FGT nanocomposites are continuously tested under current density of 1.0 A g<sup>-1</sup> for another 50 cycles. The

capacities are maintained in the range between  $\sim 1100 \text{ mAh g}^{-1}$  and  $\sim 1200 \text{ mAh g}^{-1}$ . The overall coulombic efficiency is stabilized around 100% except for the first 20 cycles due to the irreversible reaction. In conclusion,  $\text{SnO}_2$ -FGT nanocomposites exhibit good cycling performance no matter under low current density or high current density.

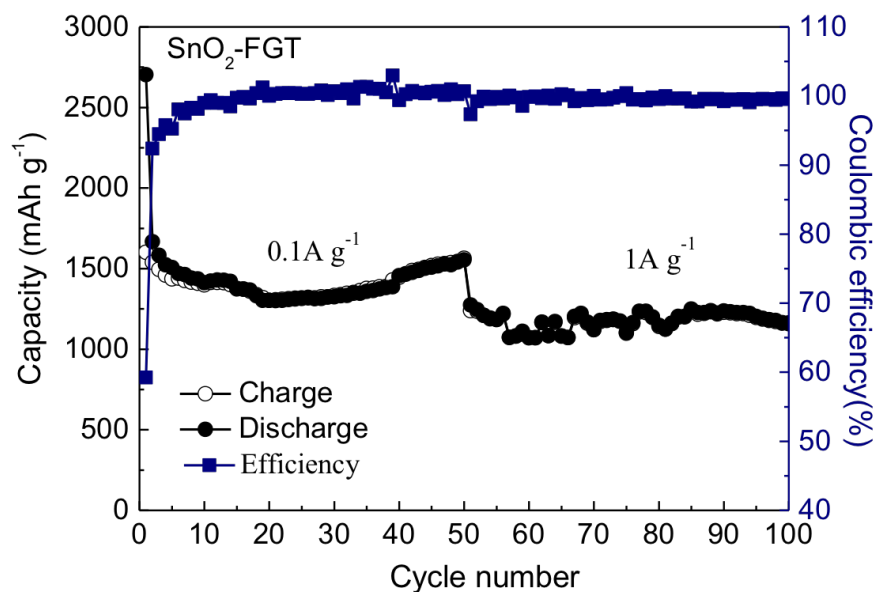


Figure 3.23 Cycle performance of  $\text{SnO}_2$ -FGT nanocomposites at different current densities of  $0.1 \text{ A g}^{-1}$  and  $1.0 \text{ A g}^{-1}$ .

The rate performance of  $\text{SnO}_2$ -FGT nanocomposites is carried under varied current densities from  $0.1 \text{ A g}^{-1}$  to  $1 \text{ A g}^{-1}$ . The average results of reversible capacities are  $\sim 1400 \text{ mAh g}^{-1}$  at  $0.1 \text{ A g}^{-1}$ ,  $\sim 1250 \text{ mAh g}^{-1}$  at  $0.2 \text{ A g}^{-1}$ ,  $\sim 1200 \text{ mAh g}^{-1}$  at  $0.5 \text{ A g}^{-1}$  and  $\sim 1100 \text{ mAh g}^{-1}$  at  $1 \text{ A g}^{-1}$ . Especially when the current density returns back to the original current density of  $0.1 \text{ A g}^{-1}$ , the average capacity is around  $1400 \text{ mAh g}^{-1}$ , which is much close to the initial test results. These results demonstrate that the special 3D structure of FGT and nanosize of  $\text{SnO}_2$  particles can improve the structural stability of

SnO<sub>2</sub>-FGT nanocomposites during fast discharging and charging, leading to tolerance to high current density with long cycling.

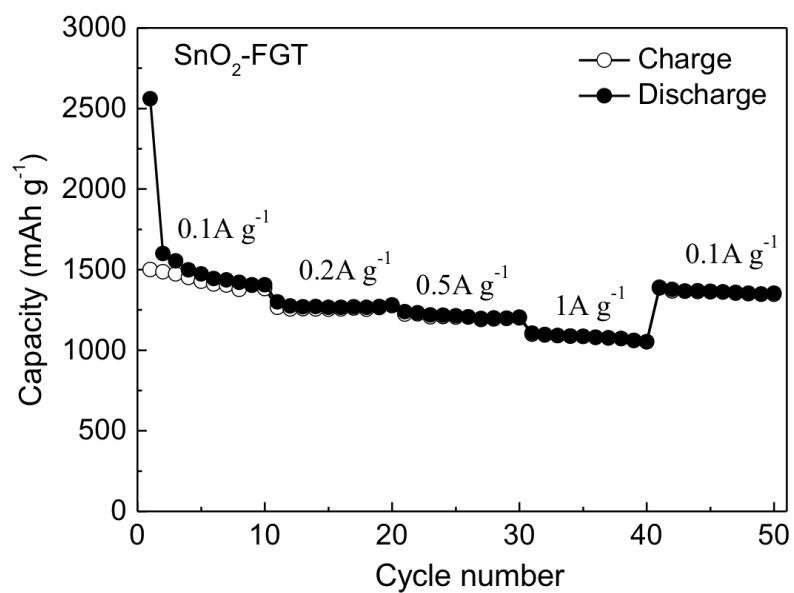


Figure 3.24 Cycle performance SnO<sub>2</sub>-FGT nanocomposites at different current densities from 0.1 A g<sup>-1</sup> to 1 A g<sup>-1</sup>.



## 4 Conclusion

In the first part of our research, a new method for Highly dispersible edge-selectively oxidized graphene was prepared. The edge-oxidization and FeCl<sub>3</sub> intercalation processes are applied to produce edge-oxidized graphene (EOG) with several layers. EOG has been confirmed that only edge part of the graphene nanosheet is oxidized by XRD and Raman spectroscopy, while the basal plane maintains the graphene structure. And the electrochemical performance of EOG as anode material shows that it has reversible capacity of ~650 mAh g<sup>-1</sup> at current density of 0.1 A g<sup>-1</sup>. Then, SnO<sub>2</sub> nanoparticles are designed to be in-situ grown on the surface of EOG. SEM shows that SnO<sub>2</sub> nanoparticles have average dimension of ~10 nm and are uniformly dispersed on the surface of EOG. As a comparison, bare SnO<sub>2</sub> nanoparticles are also synthesized. The electrochemical performance of SnO<sub>2</sub>/EOG nanocomposites and bare SnO<sub>2</sub> nanoparticles shows that SnO<sub>2</sub>/EOG nanocomposites have higher reversible capacity, around 1420 mA h g<sup>-1</sup> at 0.1 A g<sup>-1</sup>, and better cycling stability since bare SnO<sub>2</sub> nanoparticles have initial capacity of 1000 mA h g<sup>-1</sup> and keep degrading until 687 mA h g<sup>-1</sup> after 50 cycles. Moreover, EIS results demonstrate that the resistance for SnO<sub>2</sub>/EOG nanocomposites (18 Ω) is quite smaller than that of bare SnO<sub>2</sub> nanoparticles (82 Ω). These results verify that the existence of EOG can efficiently increase the electric conductivity and stabilize the structure of electrode material during repeatedly discharge and charge process.

In the second part, a novel three-dimensional graphene, called flower-like graphene tube (FGT) is designed with sheets composed tube structure. The layer structure produces high surface area and the 3D structure prevents graphene from stacking

together. In order to improve the capacity of bare graphene material, SnO<sub>2</sub> is chosen to combine with it through hydrothermal synthesis. The electrochemical performance of SnO<sub>2</sub>-FGT nanocomposites shows that it has good cycling stability at current densities of 0.1 A g<sup>-1</sup> and even as high as 1.0 A g<sup>-1</sup>, producing reversible capacities of 1400 mA h g<sup>-1</sup> and 1100 mA h g<sup>-1</sup> respectively. It is believed that the 3D structure of graphene can not only serve as a good conducting network, but also an excellent structural stability of the whole electrode material.

## Reference

- [1] Chen, J., Xu, L., Li, W., & Gou, X. (2005).  $\alpha$ -Fe<sub>2</sub>O<sub>3</sub> Nanotubes in Gas Sensor and Lithium-Ion Battery Applications. *Advanced Materials*, 17(5), 582-586. doi:10.1002/adma.200401101.
- [2] Chen, J. S., Li, C. M., Zhou, W. W., Yan, Q. Y., Archer, L. A., & Lou, X. W. (2009). One-pot formation of SnO<sub>2</sub> hollow nanospheres and  $\alpha$ -Fe<sub>2</sub>O<sub>3</sub>@SnO<sub>2</sub> nanorattles with large void space and their lithium storage properties. *Nanoscale*, 1(2), 280. doi:10.1039/b9nr00102f.
- [3] Chen, J. S., Zhu, T., Yang, X. H., Yang, H. G., & Lou, X. W. (2010). Top-Down Fabrication of  $\alpha$ -Fe<sub>2</sub>O<sub>3</sub> Single-Crystal Nanodiscs and Microparticles with Tunable Porosity for Largely Improved Lithium Storage Properties. *Journal of the American Chemical Society*, 132(38), 13162-13164. doi:10.1021/ja1060438.
- [4] Zanini, M., Basu, S., & Fischer, J. (1978). Alternate synthesis and reflectivity spectrum of stage 1 lithium—graphite intercalation compound. *Carbon*, 16(3), 211-212. doi:10.1016/0008-6223(78)90026-x.
- [5] Basu, S., Zeller, C., Flanders, P., Fuerst, C., Johnson, W., & Fischer, J. (1979). Synthesis and properties of lithium-graphite intercalation compounds. *Materials Science and Engineering*, 38(3), 275-283. doi:10.1016/0025-5416(79)90132-0.
- [6] US 4304825, Basu; Samar, "Rechargeable battery", issued 8 December 1981, assigned to Bell Telephone Laboratories.
- [7] Mizushima, K., Jones, P. C., Wiseman, P. J., & Goodenough, J. B. (1982). Li<sub>x</sub>CoO<sub>2</sub> (0 < x ≤ 1): A new cathode material for batteries of high energy density. *Ferrites*, 425-428. doi:10.1007/978-94-009-7825-6\_95.
- [8] Yazami, R., & Touzain, P. (1983). A reversible graphite-lithium negative electrode for electrochemical generators. *Journal of Power Sources*, 9(3), 365-371. doi:10.1016/0378-7753(83)87040-2.
- [9] Casas, C. D., & Li, W. (2012). A review of application of carbon nanotubes for lithium ion battery anode material. *Journal of Power Sources*, 208, 74-85. doi:10.1016/j.jpowsour.2012.02.013.
- [10] Armand, M., & Tarascon, J. (2008). Building better batteries. *Nature*, 451(7179), 652-657. doi:10.1038/451652a.
- [11] Etacheri, V., Marom, R., Elazari, R., Salitra, G., & Aurbach, D. (2011). Challenges in the development of advanced Li-ion batteries: A review. *Energy & Environmental Science*, 4(9), 3243. doi:10.1039/c1ee01598b.

- [12] Goriparti, S., Miele, E., Angelis, F. D., Fabrizio, E. D., Zaccaria, R. P., & Capiglia, C. (2014). Review on recent progress of nanostructured anode materials for Li-ion batteries. *Journal of Power Sources*, 257, 421-443. doi:10.1016/j.jpowsour.2013.11.103.
- [13] Marom, R., Amalraj, S. F., Leifer, N., Jacob, D., & Aurbach, D. (2011). A review of advanced and practical lithium battery materials. *Journal of Materials Chemistry*, 21(27), 9938. doi:10.1039/c0jm04225k.
- [14] Scrosati, B., & Garche, J. (2010). Lithium batteries: Status, prospects and future. *Journal of Power Sources*, 195(9), 2419-2430. doi:10.1016/j.jpowsour.2009.11.048.
- [15] Meunier, V., Kephart, J., Roland, C., & Bernholc, J. (2002). Ab Initio Investigations of Lithium Diffusion in Carbon Nanotube Systems. *Physical Review Letters*, 88(7). doi:10.1103/physrevlett.88.075506.
- [16] Fujimoto, H., Tokumitsu, K., Mabuchi, A., Chinnasamy, N., & Kasuh, T. (2010). The anode performance of the hard carbon for the lithium ion battery derived from the oxygen-containing aromatic precursors. *Journal of Power Sources*, 195(21), 7452-7456. doi:10.1016/j.jpowsour.2010.05.041.
- [17] Bridges, C. A., Sun, X., Zhao, J., Paranthaman, M. P., & Dai, S. (2012). In Situ Observation of Solid Electrolyte Interphase Formation in Ordered Mesoporous Hard Carbon by Small-Angle Neutron Scattering. *The Journal of Physical Chemistry C*, 116(14), 7701-7711. doi:10.1021/jp3012393.
- [18] Hou, J., Shao, Y., Ellis, M. W., Moore, R. B., & Yi, B. (2011). Graphene-based electrochemical energy conversion and storage: fuel cells, supercapacitors and lithium ion batteries. *Physical Chemistry Chemical Physics*, 2011, 13, 15384-15402. doi: 10.1039/C1CP21915D.
- [19] Kamal, A. R., Fray, D. J., Review on Carbon and Silicon Based Materials as Anode Materials for Lithium Ion Batteries. *Journal of New Materials for Electrochemical Systems*, [S.l.], v. 13, n. 2, p. 147-160, 2010, 06. ISSN 2292-1168.
- [20] Dahn, J., Sleight, A., Shi, H., Reimers, J., Zhong, Q., & Way, B. (1993). Dependence of the electrochemical intercalation of lithium in carbons on the crystal structure of the carbon. *Electrochimica Acta*, 38(9), 1179-1191. doi:10.1016/0013-4686(93)80048-5.
- [21] Matsumura, Y., Wang, S., & Mondori, J. (1995). Interactions between disordered carbon and lithium in lithium ion rechargeable batteries. *Carbon*, 33(10), 1457-1462. doi:10.1016/0008-6223(95)00098-x.
- [22] Wagemaker, M., & Mulder, F. M. (2012). Properties and Promises of Nanosized Insertion Materials for Li-Ion Batteries. *Accounts of Chemical Research*, 46(5), 1206-1215. doi:10.1021/ar2001793.

- [23] Natarajan, C., Setoguchi, K., & Nogami, G. (1998). Preparation of a nanocrystalline titanium dioxide negative electrode for the rechargeable lithium ion battery. *Electrochimica Acta*, 43(21-22), 3371-3374. doi:10.1016/s0013-4686(97)10140-2.
- [24] Balogun, M., Li, C., Zeng, Y., Yu, M., Wu, Q., Wu, M., . . . Tong, Y. (2014). Titanium dioxide@titanium nitride nanowires on carbon cloth with remarkable rate capability for flexible lithium-ion batteries. *Journal of Power Sources*, 272, 946-953. doi:10.1016/j.jpowsour.2014.09.034.
- [25] Wang, D., Choi, D., Li, J., Yang, Z., Nie, Z., Kou, R., Liu, J. (2009). Self-Assembled TiO<sub>2</sub>-Graphene Hybrid Nanostructures for Enhanced Li-Ion Insertion. *ACS Nano*, 3(4), 907-914. doi:10.1021/nn900150y.
- [26] Chen, Z., Belharouak, I., Sun, Y., & Amine, K. (2012). Titanium-Based Anode Materials for Safe Lithium-Ion Batteries. *Advanced Functional Materials*, 23(8), 959-969. doi:10.1002/adfm.201200698.
- [27] Wu, H., & Cui, Y. (2012). Designing nanostructured Si anodes for high energy lithium ion batteries. *Nano Today*, 7(5), 414-429. doi:10.1016/j.nantod.2012.08.004.
- [28] Szczech, J. R., & Jin, S. (2011). Nanostructured silicon for high capacity lithium battery anodes. *Energy Environ. Sci.*, 4(1), 56-72. doi:10.1039/c0ee00281j.
- [29] Key, B., Bhattacharyya, R., Morcrette, M., Seznéc, V., Tarascon, J., & Grey, C. P. (2009). Real-Time NMR Investigations of Structural Changes in Silicon Electrodes for Lithium-Ion Batteries. *Journal of the American Chemical Society*, 131(26), 9239-9249. doi:10.1021/ja8086278.
- [30] Wen, Z., Lu, G., Mao, S., Kim, H., Cui, S., Yu, K., . . . Chen, J. (2013). Silicon nanotube anode for lithium-ion batteries. *Electrochemistry Communications*, 29, 67-70. doi:10.1016/j.elecom.2013.01.015.
- [31] Song, T., Xia, J., Lee, J., Lee, D. H., Kwon, M., Choi, J., . . . Paik, U. (2010). Arrays of Sealed Silicon Nanotubes as Anodes for Lithium Ion Batteries. *Nano Letters*, 10(5), 1710-1716. doi:10.1021/nl100086e.
- [32] Park, C., Kim, J., Kim, H., & Sohn, H. (2010). Li-alloy based anode materials for Li secondary batteries. *Chemical Society Reviews*, 39(8), 3115. doi:10.1039/b919877f.
- [33] Rudawski, N., Yates, B., Holzworth, M., Jones, K., Elliman, R., & Volinsky, A. (2013). Ion beam-mixed Ge electrodes for high capacity Li rechargeable batteries. *Journal of Power Sources*, 223, 336-340. doi:10.1016/j.jpowsour.2012.09.056.
- [34] Chockla, A. M., Klavetter, K. C., Mullins, C. B., & Korgel, B. A. (2012). Solution-Grown Germanium Nanowire Anodes for Lithium-Ion Batteries. *ACS Applied Materials & Interfaces*, 4(9), 4658-4664. doi:10.1021/am3010253.

- [35] Liu, X. H., Huang, S., Picraux, S. T., Li, J., Zhu, T., & Huang, J. Y. (2011). Reversible Nanopore Formation in Ge Nanowires during Lithiation–Delithiation Cycling: An In Situ Transmission Electron Microscopy Study. *Nano Letters*, *11*(9), 3991-3997. doi:10.1021/nl2024118.
- [36] Kim, C. H., Im, H. S., Cho, Y. J., Jung, C. S., Jang, D. M., Myung, Y., Cho, W. (2012). High-Yield Gas-Phase Laser Photolysis Synthesis of Germanium Nanocrystals for High-Performance Photodetectors and Lithium Ion Batteries. *The Journal of Physical Chemistry C*, *116*(50), 26190-26196. doi:10.1021/jp308852g.
- [37] Xu, J., & Zhu, Y. (2012). Monodisperse Fe<sub>3</sub>O<sub>4</sub> and  $\gamma$ -Fe<sub>2</sub>O<sub>3</sub> Magnetic Mesoporous Microspheres as Anode Materials for Lithium-Ion Batteries. *ACS Applied Materials & Interfaces*, *4*(9), 4752-4757. doi:10.1021/am301123f.
- [38] Wu, C., Yin, P., Zhu, X., Ouyang, C., & Xie, Y. (2006). Synthesis of Hematite ( $\alpha$ -Fe<sub>2</sub>O<sub>3</sub>) Nanorods: Diameter-Size and Shape Effects on Their Applications in Magnetism, Lithium Ion Battery, and Gas Sensors. *The Journal of Physical Chemistry B*, *110*(36), 17806-17812. doi:10.1021/jp0633906.
- [39] Chen, J., Xu, L., Li, W., & Gou, X. (2005).  $\alpha$ -Fe<sub>2</sub>O<sub>3</sub> Nanotubes in Gas Sensor and Lithium-Ion Battery Applications. *Advanced Materials*, *17*(5), 582-586. doi:10.1002/adma.200401101
- [40] Zhu, X., Zhu, Y., Murali, S., Stoller, M. D., & Ruoff, R. S. (2011). Nanostructured Reduced Graphene Oxide/Fe<sub>2</sub>O<sub>3</sub> Composite as a High-Performance Anode Material for Lithium Ion Batteries. *ACS Nano*, *5*(4), 3333-3338. doi:10.1021/nn200493r.
- [41] Jeong, J., Choi, B. G., Lee, S. C., Lee, K. G., Chang, S., Han, Y., Huh, Y. S. (2013). Hierarchical Hollow Spheres of Fe<sub>2</sub>O<sub>3</sub>@Polyaniline for Lithium Ion Battery Anodes. *Advanced Materials*, *25*(43), 6250-6255. doi:10.1002/adma.201302710.
- [42] Reddy, M., Yu, T., Sow, C., Shen, Z., Lim, C., Subba Rao, G., & Chowdari, B. (2007).  $\alpha$ -Fe<sub>2</sub>O<sub>3</sub> Nanoflakes as an Anode Material for Li-Ion Batteries. *Advanced Functional Materials*, *17*(15), 2792-2799. doi:10.1002/adfm.200601186.
- [43] Barreca, D., Cruz-Yusta, M., Gasparotto, A., Maccato, C., Morales, J., Pozza, A., Tondello, E. (2010). Cobalt Oxide Nanomaterials by Vapor-Phase Synthesis for Fast and Reversible Lithium Storage. *The Journal of Physical Chemistry C*, *114*(21), 10054-10060. doi:10.1021/jp102380e.
- [44] Wu, Z., Ren, W., Wen, L., Gao, L., Zhao, J., Chen, Z., Cheng, H. (2010). Graphene Anchored with Co<sub>3</sub>O<sub>4</sub> Nanoparticles as Anode of Lithium Ion Batteries with Enhanced Reversible Capacity and Cyclic Performance. *ACS Nano*, *4*(6), 3187-3194. doi:10.1021/nn100740x.

- [45] Lou, X., Deng, D., Lee, J., Feng, J., & Archer, L. (2008). Self-Supported Formation of Needlelike Co<sub>3</sub>O<sub>4</sub> Nanotubes and Their Application as Lithium-Ion Battery Electrodes. *Advanced Materials*, 20(2), 258-262. doi:10.1002/adma.200702412.
- [46] Li, Y., Tan, B., & Wu, Y. (2008). Mesoporous Co<sub>3</sub>O<sub>4</sub> Nanowire Arrays for Lithium Ion Batteries with High Capacity and Rate Capability. *Nano Letters*, 8(1), 265-270. doi:10.1021/nl0725906.
- [47] Li, W. Y., Xu, L. N., & Chen, J. (2005). Co<sub>3</sub>O<sub>4</sub> Nanomaterials in Lithium-Ion Batteries and Gas Sensors. *Advanced Functional Materials*, 15(5), 851-857. doi:10.1002/adfm.200400429.
- [48] Li, B., Cao, H., Shao, J., Li, G., Qu, M., & Yin, G. (2011). Co<sub>3</sub>O<sub>4</sub>@graphene Composites as Anode Materials for High-Performance Lithium Ion Batteries. *Inorganic Chemistry*, 50(5), 1628-1632. doi:10.1021/ic1023086.
- [49] Koo, B., Xiong, H., Slater, M. D., Prakapenka, V. B., Balasubramanian, M., Podsiadlo, P., . . . Shevchenko, E. V. (2012). Hollow Iron Oxide Nanoparticles for Application in Lithium Ion Batteries. *Nano Letters*, 12(5), 2429-2435. doi:10.1021/nl3004286.
- [50] Zhu, X., Wu, W., Liu, Z., Li, L., Hu, J., Dai, H., Song, X. (2013). A reduced graphene oxide–nanoporous magnetic oxide iron hybrid as an improved anode material for lithium ion batteries. *Electrochimica Acta*, 95, 24-28. doi:10.1016/j.electacta.2013.02.029.
- [51] Lee, S. H., Mathews, M., Toghiani, H., Wipf, D. O., & Pittman, J. C. (2009). Fabrication of Carbon-Encapsulated Mono- and Bimetallic (Sn and Sn/Sb Alloy) Nanorods. Potential Lithium-Ion Battery Anode Materials. *Chemistry of Materials*, 21(11), 2306-2314. doi:10.1021/cm900640u.
- [52] Guo, B., Shu, J., Tang, K., Bai, Y., Wang, Z., & Chen, L. (2008). Nano-Sn/hard carbon composite anode material with high-initial coulombic efficiency. *Journal of Power Sources*, 177(1), 205-210. doi:10.1016/j.jpowsour.2007.11.003.
- [53] Marcinek, M., Hardwick, L., Richardson, T., Song, X., & Kostecki, R. (2007). Microwave plasma chemical vapor deposition of nano-structured Sn/C composite thin-film anodes for Li-ion batteries. *Journal of Power Sources*, 173(2), 965-971. doi:10.1016/j.jpowsour.2007.08.084.
- [54] Morishita, T., Hirabayashi, T., Okuni, T., Ota, N., & Inagaki, M. (2006). Preparation of carbon-coated Sn powders and their loading onto graphite flakes for lithium ion secondary battery. *Journal of Power Sources*, 160(1), 638-644. doi:10.1016/j.jpowsour.2006.01.087.

- [55] Wang, Y., Wu, M., Jiao, Z., & Lee, J. Y. (2009). Sn@CNT and Sn@C@CNT nanostructures for superior reversible lithium ion storage. *Chemistry of Materials*, 21(14), 3210-3215. doi:10.1021/cm900702d.
- [56] Kezhi, L., Xiaolin, W., Yanhui, X., & Guohua, L. (2006). Nano-sized Sn/MWNTs and MWNTs served as the anode of lithium ion battery. *Journal of Wuhan University of Technology-Mater. Sci. Ed.*, 21(4), 60-63. doi:10.1007/bf02841206.
- [57] Bailey, D., Skelton, W., & Smith, J. (1979). Lithium-tin phase relationships between Li<sub>7</sub>Sn<sub>2</sub> and LiSn. *Journal of the Less Common Metals*, 64(2), 233-239. doi:10.1016/0022-5088(79)90174-7.
- [58] Courtney, I. A. (1997). Electrochemical and In Situ X-Ray Diffraction Studies of the Reaction of Lithium with Tin Oxide Composites. *Journal of The Electrochemical Society*, 144(6), 2045. doi:10.1149/1.1837740.
- [59] Kamali, A. R., Fray, D. J. (2011). Tin-based materials as advanced anode materials for lithium ion batteries: a review. *Reviews on Advanced Materials Science*. 194.226.210.10.
- [60] Winter, M., & Besenhard, J. O. (2010). ChemInform Abstract: Electrochemical Lithiation of Tin and Tin-Based Intermetallics and Composites. *ChemInform*, 31(3). doi:10.1002/chin.200003257.
- [61] Zhang, W. (2011). A review of the electrochemical performance of alloy anodes for lithium-ion batteries. *Journal of Power Sources*, 196(1), 13-24. doi:10.1016/j.jpowsour.2010.07.020.
- [62] Trifonova, A. (2004). Influence of the reductive preparation conditions on the morphology and on the electrochemical performance of Sn/SnSb. *Solid State Ionics*, 168(1-2), 51-59. doi:10.1016/j.ssi.2004.01.027.
- [63] Schiotz, J. (2003). A Maximum in the Strength of Nanocrystalline Copper. *Science*, 301(5638), 1357-1359. doi:10.1126/science.1086636.
- [64] Beaulieu, L. Y., Larcher, D., Dunlap, R. A., & Dahn, J. R. (2000). Reaction of Li with Grain-Boundary Atoms in Nanostructured Compounds. *Journal of The Electrochemical Society*, 147(9), 3206. doi:10.1149/1.1393884.
- [65] Yang, J. (1999). Sub-Microcrystalline Sn and Sn-SnSb Powders as Lithium Storage Materials for Lithium-Ion Batteries. *Electrochemical and Solid-State Letters*, 2(4), 161. doi:10.1149/1.1390769.
- [66] Saint, J., Morcrette, M., Larcher, D., Laffont, L., Beattie, S., Pérès, J., . . . Tarascon, J. (2007). Towards a Fundamental Understanding of the Improved Electrochemical Performance of Silicon–Carbon Composites. *Advanced Functional Materials*, 17(11), 1765-1774. doi:10.1002/adfm.200600937.



- [67] Noh, M., Kwon, Y., Lee, H., Cho, J., Kim, Y., & Kim, M. G. (2005). Amorphous Carbon-Coated Tin Anode Material for Lithium Secondary Battery. *Chemistry of Materials*, 17(8), 1926-1929. doi:10.1021/cm0481372.
- [68] Zhang, W., Hu, J., Guo, Y., Zheng, S., Zhong, L., Song, W., & Wan, L. (2008). Tin-Nanoparticles Encapsulated in Elastic Hollow Carbon Spheres for High-Performance Anode Material in Lithium-Ion Batteries. *Advanced Materials*, 20(6), 1160-1165. doi:10.1002/adma.200701364.
- [69] Kumar, T. P., Ramesh, R., Lin, Y., & Fey, G. T. (2004). Tin-filled carbon nanotubes as insertion anode materials for lithium-ion batteries. *Electrochemistry Communications*, 6(6), 520-525. doi:10.1016/j.elecom.2004.03.009.
- [70] Park, M., Kang, Y., Wang, G., Dou, S., & Liu, H. (2008). The Effect of Morphological Modification on the Electrochemical Properties of SnO<sub>2</sub> Nanomaterials. *Advanced Functional Materials*, 18(3), 455-461. doi:10.1002/adfm.200700407.
- [71] Cheng, J., Xin, H., Zheng, H., & Wang, B. (2013). One-pot synthesis of carbon coated-SnO<sub>2</sub>/graphene-sheet nanocomposite with highly reversible lithium storage capability. *Journal of Power Sources*, 232, 152-158. doi:10.1016/j.jpowsour.2013.01.025.
- [72] Jiao, Z., Chen, D., Jiang, Y., Zhang, H., Ling, X., Zhuang, H., . . . Zhao, B. (2014). Synthesis of nanoparticles, nanorods, and mesoporous SnO<sub>2</sub> as anode materials for lithium-ion batteries. *Journal of Materials Research*, 29(05), 609-616. doi:10.1557/jmr.2014.32.
- [73] Öchsner, A., Fiedler, T., Augustin, C. Metallic Hollow Sphere Structures - Multifunctional Materials for Lightweight Applications: Types, Properties and Case Studies.
- [74] Kim, W., Hwa, Y., Jeun, J., Sohn, H., & Hong, S. (2013). Synthesis of SnO<sub>2</sub> nano hollow spheres and their size effects in lithium ion battery anode application. *Journal of Power Sources*, 225, 108-112. doi:10.1016/j.jpowsour.2012.10.030.
- [75] Cheng, J., Xin, H., Zheng, H., & Wang, B. (2013). One-pot synthesis of carbon coated-SnO<sub>2</sub>/graphene-sheet nanocomposite with highly reversible lithium storage capability. *Journal of Power Sources*, 232, 152-158. doi:10.1016/j.jpowsour.2013.01.025.
- [76] Cheekati, S. L., Xing, Y., Zhuang, Y., & Huang, H. (2011). Lithium Storage Characteristics in Nano-Graphene Platelets. *Materials Challenges in Alternative and Renewable Energy*, 117-127. doi:10.1002/9781118019467.ch12.

- [77] Dahn, J. R., Zheng, T., Liu, Y., & Xue, J. S. (1995). Mechanisms for Lithium Insertion in Carbonaceous Materials. *Science*, 270(5236), 590-593. doi:10.1126/science.270.5236.590.
- [78] Yoo, E., Kim, J., Hosono, E., Zhou, H., Kudo, T., & Honma, I. (2008). Large Reversible Li Storage of Graphene Nanosheet Families for Use in Rechargeable Lithium Ion Batteries. *Nano Letters*, 8(8), 2277-2282. doi:10.1021/nl800957b.
- [79] Pan, D., Wang, S., Zhao, B., Wu, M., Zhang, H., Wang, Y., & Jiao, Z. (2009). Li Storage Properties of Disordered Graphene Nanosheets. *Chemistry of Materials*, 21(14), 3136-3142. doi:10.1021/cm900395k.
- [80] Gerouki, A. (1996). Density of States Calculations of Small Diameter Single Graphene Sheets. *Journal of The Electrochemical Society*, 143(11). doi:10.1149/1.1837227.
- [81] Lian, P., Zhu, X., Liang, S., Li, Z., Yang, W., & Wang, H. (2010). Large reversible capacity of high quality graphene sheets as an anode material for lithium-ion batteries. *Electrochimica Acta*, 55(12), 3909-3914. doi:10.1016/j.electacta.2010.02.025.
- [82] Wu, Z., Ren, W., Xu, L., Li, F., & Cheng, H. (2011). Doped Graphene Sheets as Anode Materials with Superhigh Rate and Large Capacity for Lithium Ion Batteries. *ACS Nano*, 5(7), 5463-5471. doi:10.1021/nn2006249.
- [83] Dong, X., Wang, X., Wang, J., Song, H., Li, X., Wang, L., . . . Chen, P. (2012). Synthesis of a MnO<sub>2</sub>-graphene foam hybrid with controlled MnO<sub>2</sub> particle shape and its use as a supercapacitor electrode. *Carbon*, 50(13), 4865-4870. doi:10.1016/j.carbon.2012.06.014.
- [84] Cao, X., Shi, Y., Shi, W., Lu, G., Huang, X., Yan, Q., . . . Zhang, H. (2011). Preparation of Novel 3D Graphene Networks for Supercapacitor Applications. *Small*, 7(22), 3163-3168. doi:10.1002/smll.201100990.
- [85] Xiao, X., Liu, P., Wang, J. S., Verbrugge, M., & Balogh, M. P. (2011). Vertically aligned graphene electrode for lithium ion battery with high rate capability. *Electrochemistry Communications*, 13(2), 209-212. doi:10.1016/j.elecom.2010.12.016.
- [86] Ji, H., Zhang, L., Pettes, M. T., Li, H., Chen, S., Shi, L., . . . Ruoff, R. S. (2012). Ultrathin Graphite Foam: A Three-Dimensional Conductive Network for Battery Electrodes. *Nano Letters*, 12(5), 2446-2451. doi:10.1021/nl300528p.
- [87] Li, N., Chen, Z., Ren, W., Li, F., & Cheng, H. (2012). Flexible graphene-based lithium ion batteries with ultrafast charge and discharge rates. *Proceedings of the National Academy of Sciences*, 109(43), 17360-17365. doi:10.1073/pnas.1210072109.

- [88] Wang, W., Guo, S., Penchev, M., Ruiz, I., Bozhilov, K. N., Yan, D., . . . Ozkan, C. S. (2013). Three dimensional few layer graphene and carbon nanotube foam architectures for high fidelity supercapacitors. *Nano Energy*,2(2), 294-303. doi:10.1016/j.nanoen.2012.10.001.
- [89] Bourlinos, A. B., Georgakilas, V., Zboril, R., Steriotis, T. A., & Stubos, A. K. (2009). Liquid-Phase Exfoliation of Graphite Towards Solubilized Graphenes. *Small*,5(16), 1841-1845. doi:10.1002/smll.200900242.
- [90] Green, A. A., & Hersam, M. C. (2009). Solution Phase Production of Graphene with Controlled Thickness via Density Differentiation. *Nano Letters*,9(12), 4031-4036. doi:10.1021/nl902200b.
- [91] Khan, U., Oneill, A., Lotya, M., De, S., & Coleman, J. N. (2010). High-Concentration Solvent Exfoliation of Graphene. *Small*,6(7), 864-871. doi:10.1002/smll.200902066.
- [92] Chabot, V., Kim, B., Sloper, B., Tzoganakis, C., & Yu, A. (2013). High yield production and purification of few layer graphene by Gum Arabic assisted physical sonication. *Scientific Reports*,3(1). doi:10.1038/srep01378.
- [93] Kim, K. S., Zhao, Y., Jang, H., Lee, S. Y., Kim, J. M., Kim, K. S., . . . Hong, B. H. (2009). Large-scale pattern growth of graphene films for stretchable transparent electrodes. *Nature*,457(7230), 706-710. doi:10.1038/nature07719.
- [94] Reina, A., Jia, X., Ho, J., Nezich, D., Son, H., Bulovic, V., . . . Kong, J. (2009). Large Area, Few-Layer Graphene Films on Arbitrary Substrates by Chemical Vapor Deposition. *Nano Letters*,9(1), 30-35. doi:10.1021/nl801827v.
- [95] Marcano, D. C., Kosynkin, D. V., Berlin, J. M., Sinitskii, A., Sun, Z., Slesarev, A., . . . Tour, J. M. (2010). Improved Synthesis of Graphene Oxide. *ACS Nano*,4(8), 4806-4814. doi:10.1021/nn1006368.
- [96] Zhang, H., Wang, J., Yan, Q., Zheng, W., Chen, C., & Yu, Z. (2011). Vacuum-assisted synthesis of graphene from thermal exfoliation and reduction of graphite oxide. *Journal of Materials Chemistry*,21(14), 5392. doi:10.1039/c1jm10099h.
- [97] Park, S., & Ruoff, R. S. (2009). Chemical methods for the production of graphenes. *Nature Nanotechnology*,4(4), 217-224. doi:10.1038/nnano.2009.58.
- [98] Qiu, Y., Zhang, X., & Yang, S. (2011). High performance supercapacitors based on highly conductive nitrogen-doped graphene sheets. *Physical Chemistry Chemical Physics*,13(27), 12554. doi:10.1039/c1cp21148j.
- [99] Novoselov, K. S., Fal'ko, V. I., Colombo, L., Gellert, P. R., Schwab, M. G., & Kim, K. (2012). A roadmap for graphene. *Nature*,490(7419), 192-200. doi:10.1038/nature11458.

- [100] Chabot, V., Higgins, D., Yu, A., Xiao, X., Chen, Z., & Zhang, J. (2014). A review of graphene and graphene oxide sponge: Material synthesis and applications to energy and the environment. *Energy & Environmental Science*,7(5), 1564. doi:10.1039/c3ee43385d.
- [101] Wang, G., Shen, X., Yao, J., & Park, J. (2009). Graphene nanosheets for enhanced lithium storage in lithium ion batteries. *Carbon*,47(8), 2049-2053. doi:10.1016/j.carbon.2009.03.053.
- [102] Cao, X., Shi, Y., Shi, W., Rui, X., Yan, Q., Kong, J., & Zhang, H. (2013). Preparation of MoS<sub>2</sub>-Coated Three-Dimensional Graphene Networks for High-Performance Anode Material in Lithium-Ion Batteries. *Small*,9(20), 3433-3438. doi:10.1002/smll.201202697.
- [103] Liu, Y., Cheng, Z., Sun, H., Arandiyana, H., Li, J., & Ahmad, M. (2015). Mesoporous Co<sub>3</sub>O<sub>4</sub> sheets/3D graphene networks nanohybrids for high-performance sodium-ion battery anode. *Journal of Power Sources*,273, 878-884. doi:10.1016/j.jpowsour.2014.09.121.
- [104] Wei, W., Yang, S., Zhou, H., Lieberwirth, I., Feng, X., & Müllen, K. (2013). 3D Graphene Foams Cross-linked with Pre-encapsulated Fe<sub>3</sub>O<sub>4</sub> Nanospheres for Enhanced Lithium Storage. *Advanced Materials*,25(21), 2909-2914. doi:10.1002/adma.201300445.
- [105] Dresselhaus, M. S., Jorio, A., Hofmann, M., Dresselhaus, G., & Saito, R. (2010). Perspectives on Carbon Nanotubes and Graphene Raman Spectroscopy. *Nano Letters*, 10(3), 751-758. doi:10.1021/nl904286r.